



저작자표시-비영리-변경금지 2.0 대한민국

이용자는 아래의 조건을 따르는 경우에 한하여 자유롭게

- 이 저작물을 복제, 배포, 전송, 전시, 공연 및 방송할 수 있습니다.

다음과 같은 조건을 따라야 합니다:



저작자표시. 귀하는 원저작자를 표시하여야 합니다.



비영리. 귀하는 이 저작물을 영리 목적으로 이용할 수 없습니다.



변경금지. 귀하는 이 저작물을 개작, 변형 또는 가공할 수 없습니다.

- 귀하는, 이 저작물의 재이용이나 배포의 경우, 이 저작물에 적용된 이용허락조건을 명확하게 나타내어야 합니다.
- 저작권자로부터 별도의 허가를 받으면 이러한 조건들은 적용되지 않습니다.

저작권법에 따른 이용자의 권리는 위의 내용에 의하여 영향을 받지 않습니다.

이것은 [이용허락규약\(Legal Code\)](#)을 이해하기 쉽게 요약한 것입니다.

[Disclaimer](#)

공학박사 학위논문

**A study on microstructure
evolution of hydrogels for electrical
anisotropy and mechanical properties**

하이드로젤 미세구조 조절을 통한 전기적
비등방성과 기계적 물성에 관한 연구

2023 년 2 월

서울대학교 대학원

재료공학부

김 용 우

A study on microstructure evolution of hydrogels for electrical anisotropy and mechanical properties

지도 교수 선 정 윤

이 논문을 공학박사 학위논문으로 제출함
2022 년 12 월

서울대학교 대학원
재료공학부
김 용 우

김용우의 공학박사 학위논문을 인준함
2022 년 12 월

위 원 장 _____ 안 철 희 (인)

부위원장 _____ 선 정 윤 (인)

위 원 _____ 도 준 상 (인)

위 원 _____ 김 소 연 (인)

위 원 _____ 이 근 형 (인)

Abstract

A study on microstructure evolution of hydrogels for electrical anisotropy and mechanical properties

Yong-Woo Kim

Department of Materials Science and Engineering

The graduate School

Seoul National University

Hydrogels are hydrophilic polymer networks retaining a large amount of water. High water contents make the hydrogels dissolve a variety of polymers and salts, which make the gel resemble physiological conditions. Structural and mechanical controllability make the gel similar with the structural and mechanical properties of biological tissues. The hydrogels have naturally hydrophilicity which decrease human immune reaction comparing with hydrophobic materials. Therefore, the hydrogel can be more biocompatible,

comparing with other materials. Because of these characteristics of hydrogels, they are used in a broad of applications such as, epidermal sensor, implantable devices, tissue replacement, drug delivery, and wound healing.

In first part, to achieve desirable bioelectronic performances and functionalities for biomedical applications. high electrical anisotropy in hydrogels was achieved by modulating microstructures such as, alignment, crystallinity, pore size, phase separation, viscosity. Specifically, we design highly electrically anisotropic hydrogels in controlled microstructures depending on diverse processes. We developed sequential process comprised of: directional freezing-induced alignment process, soaking-induced infiltration process, sodium citrate-induced PVA precipitation process to make directionally aligned, conductive PEDOT:PSS-separately infiltrated, and the PEDOT:PSS-highly connected hydrogels. Here we show how we design highly electrically anisotropic hydrogels in controlled microstructures depending on diverse processes.

In second part, we designed a non-swellable hydrogel with high stiffness and toughness by interpenetrating covalently and ionically crosslinked networks. The stiffness is enhanced by utilizing ionic crosslinking sites fully, and the toughness is enhanced by adopting synergistic effects between energy-dissipation by ionic networks and crack-bridging by covalent networks. Non-swelling behaviors of the gel are achieved by densifying covalent and ionic crosslinks. The hybrid gel shows high elastic moduli (up to 108 MPa) and high fracture energies (up to $8,850 \text{ J m}^{-2}$).

In third part, furthermore, we demonstrate that toughening mechanism can be applied to functional polymer for enhanced fracture toughness without losing functionality. We synthesized a tough and thermo-sensitive hydrogel with a large actuation force by forming interpenetrating networks between covalently crosslinked poly(N-isopropylacrylamide) and ionically crosslinked alginate. Poly(N-isopropylacrylamide) was used as a thermo-sensitive material, and alginate was found to enhance the mechanical properties of the hydrogels. Due to the enhanced elastic modulus and energy dissipation in the hybrid gel, the toughness was increased by a factor of 60 over that of pure PNIPAAm gel.

Keyword : electrical anisotropy, conductive hydrogels, stiff hydrogels, tough hydrogels, non-swelling hydrogels

Student Number : 2014-22514

Table of Contents

Chapter 1. Introduction	1
1.1 Study background.....	1
1.1.1 Hydrogel as biomaterials.....	1
1.1.2 Hydrogels as electrode	2
1.1.3 Issues on hydrogel-based biomaterials.....	2
1.1.4 Requirements of hydrogel-based electrode	3
1.2 Purpose of Research	3
 Chapter 2. Anisotropically conductive hydrogels	 7
2.1 Introduction	7
2.2 Experimental section	8
2.2.1 Aligned porous PVA preparation.....	8
2.2.2 PEDOT:PSS soaking solution preparation.....	8
2.2.3 Anisotropically conductive hydrogel preparation	9
2.2.4 Conductivity measurement	9
2.3 Results and Discussion	9
2.3.1 Fabrication of anisotropically conductive hydrogels	9
2.3.2 Microstructure depending on process	10
2.3.3 Alignment.....	11
2.3.4 Phase separation.....	11
2.3.5 Sodium citrate-induced PVA precipitation.....	12
2.3.6 Sodium citrate-induced PSS elimination	13
2.3.7 PEDOT-grain aggregation	14

2.3.8 Synergistic effect of sodium citrate treatment for electrical anisotropy	14
2.3.9 Electrical property and their anisotropy depending on microstructure	15
2.3.10 Porosity	15
2.3.11 Viscosity	16
2.4 Conclusion	39
Chapter 3. Enhanced mechanical properties of hydrogels	40
3.1 Introduction	40
3.2 Experimental section	42
3.2.1 Gel preparation.....	42
3.2.2 Tensile test preparation	43
3.2.3 Fracture test preparation.....	44
3.2.4 <i>in vitro</i> swelling test	44
3.2.5 <i>in vivo</i> swelling test.....	45
3.2.6 Live/dead staining	45
3.3 Results and Discussion	46
3.3.1 Fabrication	46
3.3.2 Hybrid gels.....	48
3.3.3 Stiffness and toughness	48
3.3.4 Fe ³⁺ ionic crosslinking density effect.....	49
3.3.5 Covalent crosslinking density effect.....	50
3.3.6 Polymer ratio effect.....	51
3.3.7 <i>in vitro</i> swelling test	51

3.3.8 <i>in vivo</i> swelling test.....	52
3.3.9 Cytotoxicity test.....	53
3.4 Conclusion.....	71
3.5. Reference.....	72
 Chapter 4. Enhanced mechanical properties of functional hydrogels	74
4.1 Introduction	74
4.2 Experimental section	76
4.2.1 Gel preparation.....	76
4.2.2 Mechanical test preparation	77
4.2.3 Thermo-sensitive behavior test preparation.....	77
4.3 Results and Discussion.....	78
4.4 Conclusion.....	92
4.5 Reference.....	93
 Bibliography.....	95
 Abstract in Korean	96

List of Figures

Figure 1.1	Hydrogels resemble with native extracellular environment	4
Figure 1.2	Structural and mechanical similarity of hydrogels with biological tissues.....	5
Figure 1.3	Hydrogels have a broad of applications.....	6
Figure 2.1	Fabrication of anisotropically conductive hydrogels.....	19
Figure 2.2	Photographs of PVA-PEDOT:PSS hydrogels.....	20
Figure 2.3	Measurement setup for anisotropically conductive hydrogels	21
Figure 2.4	Anisotropic conductivity	22
Figure 2.5	Effects of fabrication-process on microstructures	23
Figure 2.6	DSC profiles depending on fabrication-process	24
Figure 2.7	SEM images that show directionally aligned porous, pure PVA.....	25
Figure 2.8	FTIR spectra of pure PVA dependent of freezing directionality and citrate treatment	26
Figure 2.9	Washing tests for PEDOT:PSS aggregation by sodium citrate treatment	27
Figure 2.10	X-ray S 2 <i>p</i> photoelectron spectra of pure PEDOT:PSS dependent of citrate treatment	28
Figure 2.11	Soaking time effects for anisotropic conductivity	29
Figure 2.12	WAXS for PVA-PEDOT:PSS dependent of citrate treatment	30
Figure 2.13	Parallel and perpendicular resistance of PVA-PEDOT:PSS as a	

function of sodium citrate concentration	31
Figure 2.14 Effects of fabrication–process on anisotropic conductivity...	32
Figure 2.15 Effects of compositions on anisotropic conductivity	33
Figure 2.16 Aligned porous, pure PVA with directional freezing	34
Figure 2.17 Apparency depending on PVA concentration	35
Figure 2.18 SEM images of pure PVA.....	36
Figure 2.19 Apparent viscosity of pure PEDOT:PSS	37
Figure 2.20 X-ray photoelectrons spectroscopy (XPS) S 2 <i>p</i> spectra for PEDOT:PSS.....	38
Figure 3.1 The hybrid hydrogels are obtained by the stepwise crosslinking of two different polymer systems.	54
Figure 3.2 Images of pHEMA-alginate hydrogels in each step.....	55
Figure 3.3 We compared the pHEMA-alginate hybrid hydrogels during the different reaction steps.....	56
Figure 3.4 Tensile test specimen configuration	57
Figure 3.5 Comparison of pHEMA gel, alginate gel, and pHEMA-alginate gel in stress-stretch curves.....	58
Figure 3.6 A demonstration of high stiffness and toughness for the pHEMA-alginate hydrogels.....	59
Figure 3.7 Ionic crosslinks effects	60
Figure 3.8 Covalent crosslinks effects.....	61
Figure 3.9 Polymer ratio effects.	62
Figure 3.10 Fracture tests introduced by Rivlin and Thomas.....	63

Figure 3.11 Fracture tests were performed with notched gels.....	64
Figure 3.12 Elastic modulus versus fracture energy plots for a variety of materials.....	65
Figure 3.13 <i>in vitro</i> swelling behaviors.	66
Figure 3.14 Elastic modulus of the gel was measured as a function of ion release time in a DPBS solution.	67
Figure 3.15 <i>in vivo</i> swelling behaviors were monitored via hydrogel implantation in rats.	68
Figure 3.16 Evaluation of cell viability in gel-conditioned media.	69
Figure 3.17 Cell viability percentage as a function of gel-conditioning times for a variety of gels.	70
Figure 4.1 Pure active materials are weak.....	83
Figure 4.2 Active materials must be tough.....	84
Figure 4.3 Tensile tests of PNIPAAm-alginate hybrid gel	85
Figure 4.4 Fracture tests of PNIPAAm-alginate hybrid gel.....	86
Figure 4.5 Fracture toughness measurements of hybrid gel.....	87
Figure 4.6 Thermo-sensitive behaviors of hybrid gel.....	88
Figure 4.7 Phase transition	89
Figure 4.8 Comparison of equilibrium lengths at temperature T	90
Figure 4.9 Equilibrium swelling ratio.....	91

Chapter 1. Introduction

1.1 Study Background

1.1.1 Hydrogels as biomaterials

Tissue engineering is a set of combinational disciplines that can repair, preserve, and replace damaged or diseased tissues or enhance tissue function. Biomimetic scaffolds recapitulating the properties of the *in vivo* extracellular matrix (ECM) provides biochemical (functionality, ion diffusion) and biophysical signals (stiffness, topography) that regulate cell behaviors and function (Fig. 1). The ECM is a three-dimensional network consisting of extracellular macromolecular and such as collagen, enzymes, and glycoproteins that provide structural and biochemical support to surrounding cells (Fig. 1). The filamentous nature of the ECM plays an important role in its transport properties, mechano-transduction, and growth factor signaling by interacting with cell surface receptors, binding growth factors, and signaling proteins.

Hydrogels are hydrophilic polymer networks retaining a large amount of water (Fig. 1). High water contents make the hydrogels dissolve a variety of polymers and salts, which make the gel resemble physiological conditions. Structural and mechanical controllability make the gel make similar with the structural and mechanical properties of biological tissues (Fig. 2). The hydrogels have naturally hydrophilicity which decrease human immune reaction comparing with hydrophobic materials. Therefore, the hydrogel can be more biocompatible compare with other materials. Because of these characteristics of hydrogels, they are used in a broad of applications such as, epidermal sensor, implantable devices, tissue replacement, drug delivery, and wound healing (Fig. 3).

1.1.2 Hydrogels as electrode

Biological tissue is typically considered a volume conductor with moderate conductivity (e.g., electrical conductivity $\sigma = 0.1$ to 1 sm^{-1}) in an electrical model due to mobile ionic species dissolved in the medium. Electrical communication between nerve cells depends mostly on ion fluxes because electrons cannot act as charge carriers in electrolytic tissue media. Electrodes were the most used terminals to establish electrical communication between nerve tissue and external electronic devices, allowing signals and information to be transmitted from cells to electronic devices or vice versa. Unlike biological tissues, however, almost all existing electronic systems rely on electronically conductive materials, such as metals, where free electrons act as transfer charge carriers. This characteristic difference introduces a unique interface between the electrodes and the tissue where the ion and electron transport signals are exchanged.

1.1.3 Issues on hydrogel-based biomaterials

With close similarity to biological tissues, hydrogels have attracted growing interest in the field of tissue engineering. However, there are critical problem which acts as one of the major sources of neuroinflammatory responses and corresponding failures in tissue replacement applications because of mismatch of physical and mechanical properties between synthetic hydrogels and human tissues.

Human skin exhibits high stiffness of up to 100 MPa and high toughness of up to $3,600 \text{ J m}^{-2}$ despite its high water content of 40–70 wt.%. Engineering hydrogels have rarely possessed both high stiffness and toughness because compliant hydrogels usually become brittle when excess crosslinker is added to make the gel stiff. Furthermore, conventional hydrogels usually swell under physiological conditions,

weakening their mechanical properties.

1.1.4 Requirement on hydrogels-based electrode

In hydrogel bioelectronics, the hydrogels form interfaces not only with the biological tissues but also with the electronic systems, typically in the form of metallic electrodes, interconnects, and external terminals. Together with hydrogel–tissue interfaces, hydrogel-device interfaces also play a critical role in order to achieve desirable bioelectronic performances and functionalities. However, conventional hydrogels have isotropic structure, thereby the hydrogels exhibit isotropic conduction with losing of electrical signal.

1.2 Purpose of Research

This dissertation covers research on microstructure evolution of hydrogel for electrical and mechanical properties. The dissertation is composed of two parts in large. In the first part, electrical anisotropy in hydrogels was studied with misstructure evolution. High electrical anisotropy is was achieved, so that we anticipated that this highly anisotropic conductive hydrogels can applied to bioelectronics with efficient transmittance of electrical signal and information. In the second part, we demonstrate non-swellaable, cytocompatible, stiff, and tough hydrogels. the hybrid gel shows high elastic moduli (up to 108 MPa) and high fracture energies (up to $8,850 \text{ J m}^{-2}$). In vitro and in vivo swelling tests prove non-swelling behaviors of the gel. Live/dead assays show 99% cell viability over a period of 60 days. Furthermore, we demonstrate that toughening mechanism can be applied to functional polymer for enhanced fracture toughness without losing functionality.

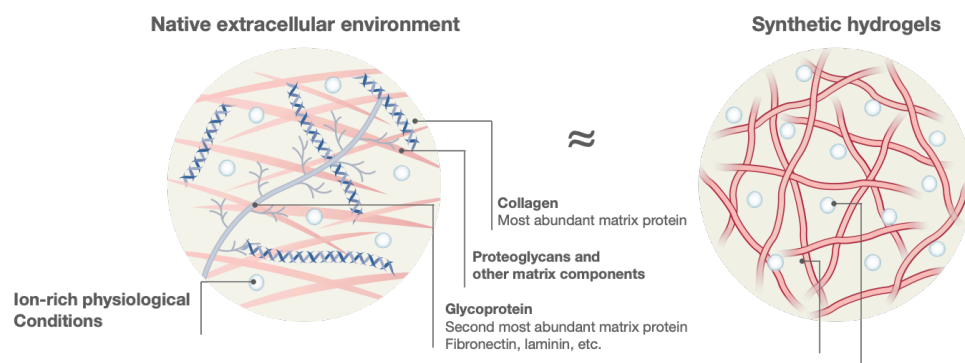


Figure 1. Hydrogels resemble with native extracellular environment.

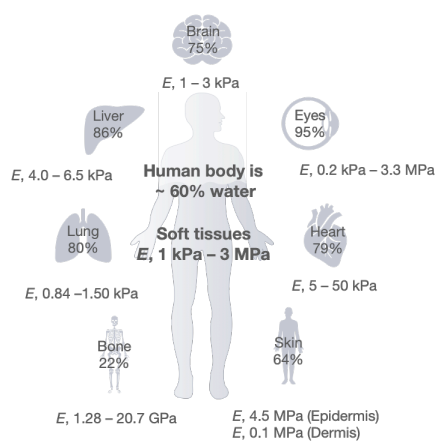


Figure 2. Structural and mechanical similarity of hydrogels with biological tissues.

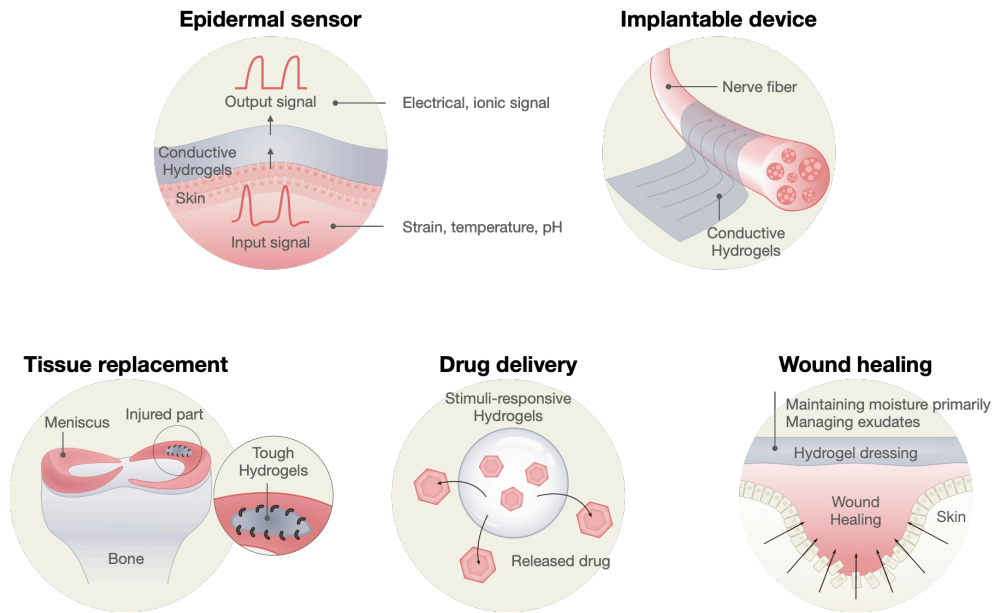


Figure 3. Hydrogels have a broad of applications.

Chapter 2. Anisotropically conductive hydrogels

2.1 Introduction

Anisotropy—the properties of being directionally dependent—has been shown in essential functions in human body systems (i.e., neural signal transmission, blood circulations, cardiac and skeletal muscle contractions). For the functional anisotropy in tissues, it is essential to have structural anisotropy. Especially, electrical anisotropy of nerve fibers was achieved by separating axon (; conductive materials) with myelin (; insulating materials) in anisotropic structure, which is rarely seen in synthetic, soft (conductive) materials.

Hydrogels—hydrophilic polymer networks retaining a large amount of water—are soft, conductive by dissolving salts, so that they have been studied as soft electrodes for wearable devices and implantable devices. However, many hydrogels have isotropic structure, thereby exhibiting electrical isotropy. Thus, for anisotropy in conduction, structural anisotropy should be introduced into hydrogels by using microstructure control such as, alignment, crystallinity, phase separation, porosity, entanglement, and swelling. For example, alignment methods such as directional freezing, mechanical stretching, magnetic field applying, and delignified cellulose fiber utilizing could be used to allow the hydrogels have anisotropic structure. The aligned hydrogels have been studied for mechanical properties. However, they have shown low electrical anisotropy due to electrical signal along undesired direction caused by homogeneous phase of conductive and insulating material. For high electrical anisotropy where electrical signal transmits along designated direction, molecular alignment must be integrated with phase separation, and other microstructure control may be further integrated if necessary.

Here, we report highly anisotropic conductive hydrogels based on microstructure control which is integrated from: (1) methods controlling structural anisotropy, which is attained achieved by directional freezing offering alignment directionality; and (2) elements providing additional microstructure modifications: An important element is phase separation accomplished induced by sequential process. Other elements are porosity and crystallization activated by precipitation thorough sodium citrate treatment.

2.2. Experimental section

2.2.1 aligned porous PVA preparation

PVA solutions were prepared by dissolving PVA powder in deionized water under vigorous stirring and heating (80 °C). The homogeneous solution was poured into an acrylic mold with a copper bottom for good thermal conductor, followed by sealing with styrene foam as a peripheral thermal insulator. The sealed mold was submerged in liquid nitrogen bath for an hour. The frozen gel then was dried with freeze-drier.

2.2.2 PEDOT:PSS soaking solution preparation

PEDOT:PSS aqueous solution (1.0-1.3% solid content, Clevios PH1000, Heraeus) was stirred vigorously for 6 h at room temperature and filtered using PVDF Syringe filters (0.45 μm pore size, Chmlab). The filtered PEDOT:PSS aqueous solution was cryogenically frozen by storing in deep freezer (-80 °C) for an hour. The cryogenically frozen was lyophilized using freeze dryer (MLB-9003, Mareuda) for 3 days. The fully dried PEDOT:PSS solute was minced, followed by dissolved with deionized water a variety of concentrations.

2.2.3 Anisotropic conductive hydrogel preparation

The aligned porous PVA were submerged into PEDOT:PSS solutions for 2 days, and then immersed into a 1.5 M citric acid trisodium salt (C3674, Sigma Aldrich) solution for 4 days.

2.2.4 Conductivity measurement

Conductivity measurements were performed on a digital multimeter (34461A, Keysight) using a four-point probe with 0.5 mm platinum wire (Thermo Fisher). The conductivity is calculated by $\sigma = (I \times L) / (V \times W \times T)$, where I is the current running through probe 1 and 4, V is the potential difference between probe 2 and 3, L is the distance between the probe 2 and 3, W is the width of the sample, and T is the thickness of the sample.

2.3. Results and Discussion

2.3.1 Fabrication of anisotropically conductive hydrogels

Considering that neural fiber of white matter have anisotropic structure with insulating materials, from which conductive materials separated, resulting in electrical anisotropy, we developed a sequential process to produce highly anisotropic conductive hydrogels by achieving polymer alignment and phase separation simultaneously (Fig. 1.1). Through directional freezing-induced alignment process, aligned and porous PVA matrix were fabricated as insulating materials (Fig. 1.1, a and b). During the directional freezing, aligned PVA chains were expelled from the forming ice and entrapped within channels between directionally growing ice crystals (Fig. 1.1 b, i). Afterwards, the ice was sublimated by freeze drying process (also known as lyophilization), so that a PVA matrix whose microstructure is a negative replica of the ice is produced (Fig. 1.1 b, ii).

The PVA matrix then was filled with PEDOT:PSS to fabricate electrically conductive materials via soaking process using commercially available aqueous PEDOT:PSS solution, wherein PEDOT are hydrophobic conjugated moieties, and PSS are hydrophilic moieties (Fig. 1.1 c). By sodium citrate–induced PVA precipitation process (Fig. 1.1 d), the aligned, concentrated PVA chains were crystallized, and simultaneously the directional pores between the aligned PVA chains were size–decreased, resulting in PEDOT:PSS chains which were infiltrated in directional pores were highly connected along the long axis of pore. The resulting hydrogels exhibit alignment directionality with straight-line pattern along the direction of directional freezing, comparing with the hydrogels by non-directional freezing (Fig. 1.2). Electrical conductivities in the directions parallel (σ_{\parallel}) and perpendicular (σ_{\perp}) to the alignment direction were measured with 4-point probe method using multimeter (Fig. 1.3) to evaluate the dependence of alignment directionality on conductivity directionality. The conductivity measurements revealed that hydrogels fabricated by non-directional freezing did not have conductivity directionality because of absence of alignment directionality, whereas the directional freezing–induced hydrogels, which have alignment directionality, exhibit conductivity directionality with ~ 100 in electrical anisotropy ratio ($\sigma_{\parallel}/\sigma_{\perp}$) (Fig. 1.4).

2.3.2 Microstructure depending on process

The high electrical anisotropy is attributed that microstructure depending on process affects electrical property (Fig. 1.5). We developed sequential process comprised of: (i) directional freezing–induced alignment process, (ii) soaking–induced infiltration process, (iii) sodium citrate–induced PVA precipitation process (Fig. 1.5 a–d, denoted by process 1) to make directionally aligned, conductive PEDOT:PSS–separately infiltrated, and the PEDOT:PSS–highly

connected hydrogels.

2.3.3 Alignment

In this way, we attained a lamellar microstructure with pores between lamellae that vary over one order of magnitude from 1 to 10 μm while affecting the aligned, layered architecture (Fig. 1.5 m and q). Instead of directional freezing-induced alignment process (Fig. 1.5 b) of process 1 (Fig. 1.5 a–d), non-directional freezing proceeded (Fig. 1.5 g), and the rest of the process was all the same (Fig. 1.5 a, g–i, denoted by process 2). Then the final material is obtained with non-lamellar microstructure with pore size ranging from 10 to 30 μm , whose pore between lamellae were interconnected in the random orientation (Fig. 1.5 o). Comparison of photograph (Fig. 1.5 q and s), as well as micrograph, indicates difference in microstructure. Directional freezing-induced lamellar structure have enough space to infiltrate PEDOT:PSS because the space is made of polymers expelled by growing ice crystal, whereas non-directional freezing method do not allow enough time to expel polymers, exhibiting semi-transparent appearance due to the absence of PEDOT:PSS (Fig. 1.5 s). Differential scanning calorimetry (DSC) results (Fig. 1.6) indicate that significant difference in crystallinity was not observed between directional and non-directional methods, which means the transparent appearance in process 3 is not attributed to the extent of crystallization.

2.3.4 Phase separation

Through soaking-induced infiltration process (Fig. 1.5 c) of process 1 (Fig. 1.5 a–d), conductive PEDOT:PSS was separately infiltrated into aligned, porous, insulating PVA matrix. On the other hand, in process 4 (Fig. 1.5 a, j–l) which starts with a

homogeneous solution of PEDOT:PSS and PVA (Fig. 1.5 a and j), conductive and insulating polymers do not separated each other, although directional freezing (Fig. 1.5 k) and sodium citrate treatment (Fig. 1.5 l) processes progress afterward, and as a result conductive PEDOT:PSS-less connected hydrogels were produced (Fig. 1.5 l) with lamellar microstructure (Fig. 1.5 p), whose some lamellae were collapsed and inter-overlapped (denoted by white arrow). Moreover, the hydrogels rarely exhibit straight-line pattern by alignment directionality as shown in photograph of final product by process 4 (Fig. 1.5 t).

2.3.5 Sodium citrate-induced PVA precipitation

As previously mentioned, by sodium citrate-induced PVA precipitation process (Fig. 1.1 d) of process 1 (Fig. 1.1 a–d), sodium citrate have best ability for PVA precipitation based on lyotropic series—relative effectiveness of different ions on the precipitation of certain polymers, by which the aligned, concentrated PVA chains were precipitated with densification of lamellae, and simultaneously the directional pores between the densified lamellae were size-decreased (Fig. 1.7). Fourier-transform infrared (FTIR) spectroscopy (Fig. 1.8) of non-aligned, aligned, and aligned–sodium citrate treated PVA showed stretching vibration due to O–H moieties at 3296, 3285, and 3275 cm^{-1} , respectively. When PVA chains were treated by sodium citrate, allowing strong hydrogen bonds between the hydroxyl groups along the PVA chains approaching each other, the O–H vibrational bands shift to the lower wavenumbers, indicating that PVA chains hydrogen bonded to form its PVA precipitation. As a result of the PVA precipitation by sodium citate treatment, PEDOT:PSS chains which were infiltrated in directional pores were highly connected along the long axis of pore (Fig. 1.1 d). Washing tests (Fig. 1.9) for

PEDOT:PSS infiltrated in porous PVA depending on sodium citrate treatment. When PVA chains were treated by sodium citrate, allowing size of directional pores between the densified lamellae decreased, the PEDOT:PSS which were infiltrated in the directional pores were aggregated, indicating that the aggregated PEDOT:PSS was entrapped into confined pores. As a result, PEDOT:PSS was washed out of spacious pores without sodium citrate treatment. The above results suggest that soaking-induced infiltration process takes precedence over sodium citrate-induced PVA precipitation process as shown in process 1 (Fig. 1.1 c and d). Otherwise, as shown in process 2 (Fig. 1.1 a, b, e, and f), PEDOT:PSS chains are unable to infiltrate into confined PVA pores when sodium citrate-induced PVA precipitation process takes priority over soaking-induced infiltration process (Fig. 1.1 e and f). Scanning electron micrograph (SEM) images (Fig. 1.1 n) reveals that bridges by interconnections between adjacent PVA lamellae, which indicate that PEDOT:PSS is excluded. As a result, photograph (Fig. 1.1 r) present that the hydrogels with process 2 shows similar appearance to pure PVA due to low contents of PEDOT:PSS.

2.3.6 Sodium citrate-induced PSS elimination

We report additional sodium citrate effect. X-ray photoelectron spectroscopy (XPS) analysis (Fig. 1.10) for pure PEDOT:PSS and sodium citrated-treated PEDOT:PSS revealed that acidic treatment by sodium citrate can remove insulating PSS chains from PEDOT chains, and as a result electrical conductivities in the directions parallel (σ_{\parallel}) to the alignment direction increased as a function of sodium citrate soaking time, comparing with that in perpendicular direction (σ_{\perp}) (Fig. 1.11).

2.3.7 PEDOT-grain aggregation

2D transmission wide-angle X-ray scattering (2D TR-WAXS) spectra (Figure 1.12) of PEDOT:PSS-separately infiltrated PVA samples depending on sodium citrate treatment. For sodium citrate-treated sample comparing with pristine, increases in the intensity were observed. The weak peak at $q = 0.82 \text{ \AA}^{-1}$ is assigned to the d_{100} alternate lamella stacking distance of PSS to PSS of 7.91 \AA . The peak at $q = 1.38 \text{ \AA}^{-1}$ shows the d_{001} spacing of PSS benzene ring π - π stacking of 4.9 \AA . The final peak at $q = 3.88 \text{ \AA}^{-1}$ represents the d_{010} reflection of PEDOT thiophene ring π - π stacking with a spacing distance of 3.6 \AA .

2.3.8 Synergistic effect of sodium citrate treatment for electrical anisotropy

Resistances in the directions parallel (Ω_{\parallel}) and perpendicular (Ω_{\perp}) to the alignment direction were plotted as a function of sodium citrate concentrations (Figure 1.13). Perpendicular resistance (Ω_{\perp}) is increased as a function of sodium citrate concentrations, because sodium citrate induced PVA precipitation process allow PVA lamellae do densify, insulating conductive path perpendicular to direction of PVA alignment. Parallel resistance (Ω_{\parallel}) is decreased as a function of sodium citrate concentrations, because sodium citrate-induced PVA precipitation process allow size of pore between the densified lamellae decreased, aggregating the infiltrated PEDOT:PSS. Furthermore, sodium citrate can remove insulating PSS chains from PEDOT aggregation, as a result PEDOT:PSS were highly connected along the alignment direction. These three effects work synergistically to enhance electrical anisotropy by high interconnecting between PEDOT grains along with aligned PVA

microchannel and insulating conductive path perpendicular to direction of PVA alignment.

2.3.9 Electrical property and their anisotropy depending on microstructure

In terms of parallel conductivity (denoted by dark gray) (Fig. 1.14 a). Directionally aligned, conductive PEDOT:PSS–separately infiltrated, and the PEDOT:PSS-highly connected hydrogels (process 1) exhibit highest conductivity, and in the following order, conductive PEDOT:PSS-less connected hydrogels due to starting from a conductive and insulating–mixed solution (process 4), non-directional freezing-induced randomly oriented hydrogel (process 3), and the hydrogels with sodium citrate treatment process taking priority over infiltration process (process 2). On the other hand, in terms of perpendicular conductivity (denoted by light gray), conductivity is in the following order: process 4, 1, 3, and 2. Consequently, Electrical anisotropy is highest in process 1 (Fig. 1.14 b).

2.3.10 Porosity

We investigated the composition conditions of PVA pre-solution concentrations and PEDOT:PSS soaking solution concentrations for electrical properties and their anisotropy (Fig. 1.15 a–d). The lamellated PVA fabricated from a variety of PVA solution concentrations were soaked in 1 wt.% in PEDOT:PSS soaking solution concentrations. Conductivities parallel (σ_{\parallel}) and perpendicular (σ_{\perp}) to the alignment direction were measured as a function of PVA pre-solution concentrations (Fig. 1.15 a). At the concentration of 4 wt.% PVA pre-solution, the measured conductivity

parallel to the alignment direction is 50–100 S m⁻¹ which are 80 times higher than 1 S m⁻¹ of conductivity in perpendicular to the alignment direction (Fig. 1.15 a,b). After the critical value of 4 wt.%, parallel conductivities were steeply decreased whereas perpendicular conductivity gradually decreased. From 5 to 8 wt.% of PVA pre-solution, both parallel and perpendicular conductivities decreased gently, so that the ratio of parallel to perpendicular to the alignment direction is also decreased moderately. At the 10 wt.%, parallel and perpendicular conductivities were decreased, the ratio of parallel to perpendicular having same ratio with that at 8 wt.% PVA pre-solution. Below 4 wt. % in the PVA pre-solution concentrations, the produced PVA microstructures were too fragile, and unidirectional microstructures were not formed (Fig. 1.16). Above 10 wt.%, pore size of lamellated PVA were too small to infiltrate PEDOT:PSS, so that they exhibits similar appearance with pure PVA (Fig. 1.17). The above results indicate that the higher the concentration of PVA pre-solution, the more number of channels, which suggests that pore size become more confined to infiltrated PEDOT:PSS (Fig. 1.18).

2.3.11 Viscosity

Conductivities regarding contents of infiltrated conductive materials were studied by fixing the value of 4 wt.% of PVA pre-solution concentration, indicating that aligned pore size were preset (Fig. 1.15 c and d). Perpendicular conductivity was irrelevant to the PEDOT:PSS soaking solution concentrations, which suggest that crystallized, aligned PVA channel walls block conductive path of PEDOT:PSS. Meanwhile, parallel conductivity was affected by the PEDOT:PSS solution concentrations. At 0.5 wt.% of diluted PEDOT:PSS solution, conductivities parallel and perpendicular to the alignment direction have no difference in conductivities, so

that they have around 1 of conductivity ratio. At 1 wt.% of pristine PEDOT:PSS solution, parallel conductivity values were around 50-100, so that conductivity ratio was 50–100. At 2 wt.%, parallel conductivity was steeply decreased. After 2 wt.%, as PEDOT:PSS concentration was increased, parallel conductivity was smoothly decreased, conductivity ratio decreasing gradually. According to the Hugging's equation,

$$\frac{\eta_s}{c} = [\eta] + \kappa_H [\eta]^2 c$$

Where η_s is the specific viscosity of a solution at a given concentration of a polymer in solution, $[\eta]$ is the intrinsic viscosity of the solution, κ_H is the Huggins coefficient, and c is the concentration of the polymer in solution. Polymer solutions show dependence of concentration on the viscosity, which supports the premise that polymer coils start to aggregate and entangle through interchain attraction force as concentration increases, which is validated by viscosity measurement (Fig. 1.19). Based on the above results, we can hypothesize that the infiltrated PEDOT:PSS existing in PVA microchannels may be sparsely remained if aggregation size of polymers in concentrated PEDOT:PSS solutions is over than channel size. Figure 1.20 a–e summarizes the XPS peak intensities as a function of binding energy for a variety of PEDOT:PSS soaking solution concentrations. In the range of 161–173 eV (S 2p), XPS spectra were fitted with symmetric/asymmetric Gaussian-Lorentzian function. The first peak (171–167 eV) reflect sulfur atoms from the styrene sulfonate (shades of yellow) and the second peak (167–163 eV) detects the absorption sulfur atoms from the EDOT thiophene (shades of blue). Binding energy scan reveal that the relative amount of PEDOT to PSS was not significant different through PEDOT:PSS concentrations (Fig. 1.20 f), validating the trend in contents of

PEDOT:PSS existent in aligned porous PVA microstructures shows good consistency with the trend in parallel conductivity (Fig. 1.20 g).

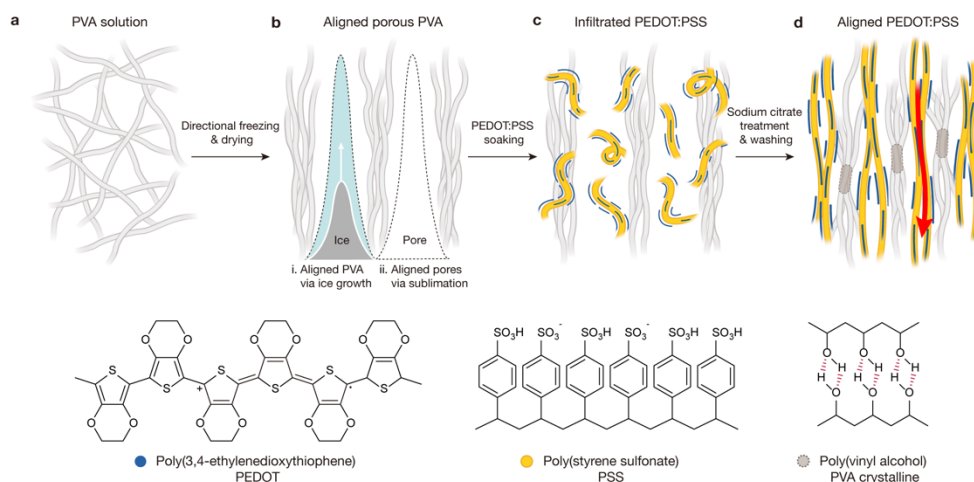


Figure 2.1 Fabrication of anisotropically conductive hydrogels.

(a) Starting solution, PVA solutions. (b) Aligned porous PVA were fabricated by directional freeze drying, in which (i) growing ice crystal expel PVA polymers, creating aligned microstructure oriented in a direction parallel to the movement of the freezing front. (ii) Afterwards, the ice was sublimated by freeze drying. (c) The aligned porous insulating PVA scaffold are infiltrated with conductive PEDOT:PSS. (d) Aligned PEDOT:PSS were obtained by Sodium citrate treatment whereby the aligned PVA were precipitated, randomly infiltrated PEDOT:PSS being oriented in the direction parallel to the precipitating PVA alignment.

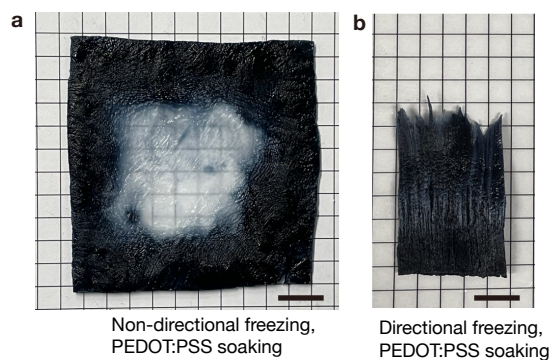
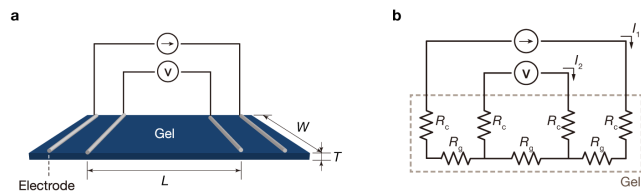


Figure 2.2 Photographs of PVA-PEDOT:PSS hydrogels.

PEDOT:PSS/PVA hydrogels were fabricated by (a) nondirectional freezing and (b) directional freezing.



$$\text{Conductivity, } \sigma = \frac{I \times L}{V \times W \times T}$$

$$L = 20 \text{ mm}, \quad W = 10 \text{ mm}, \quad T = 0.3 \sim 0.7 \text{ mm}$$

Figure 2.3 Measurement setup for anisotropically conductive hydrogels.

(a) Four-point probe setup for electrical conductivity measurement of anisotropically conductive hydrogels. (b) An electrical circuit diagram of the anisotropically conductive hydrogels with four-point probe setup.

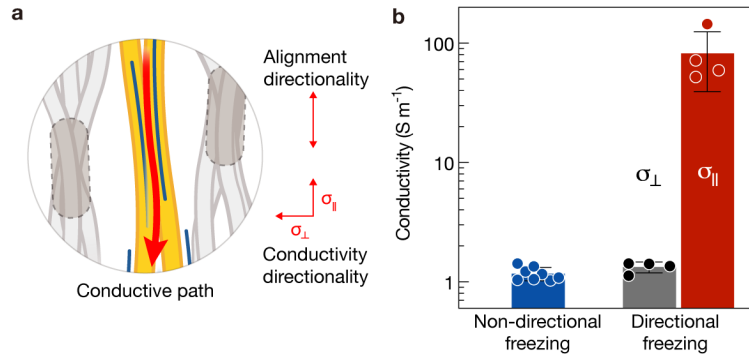


Figure 2.4 Anisotropic conductivity.

(a) σ_{\parallel} and σ_{\perp} indicate that electrical conductivity in the directions parallel and perpendicular to the alignment direction, respectively. (b) Conductivity directionality depends on freezing directionality affecting alignment direction. Scale bars indicate 10 mm.

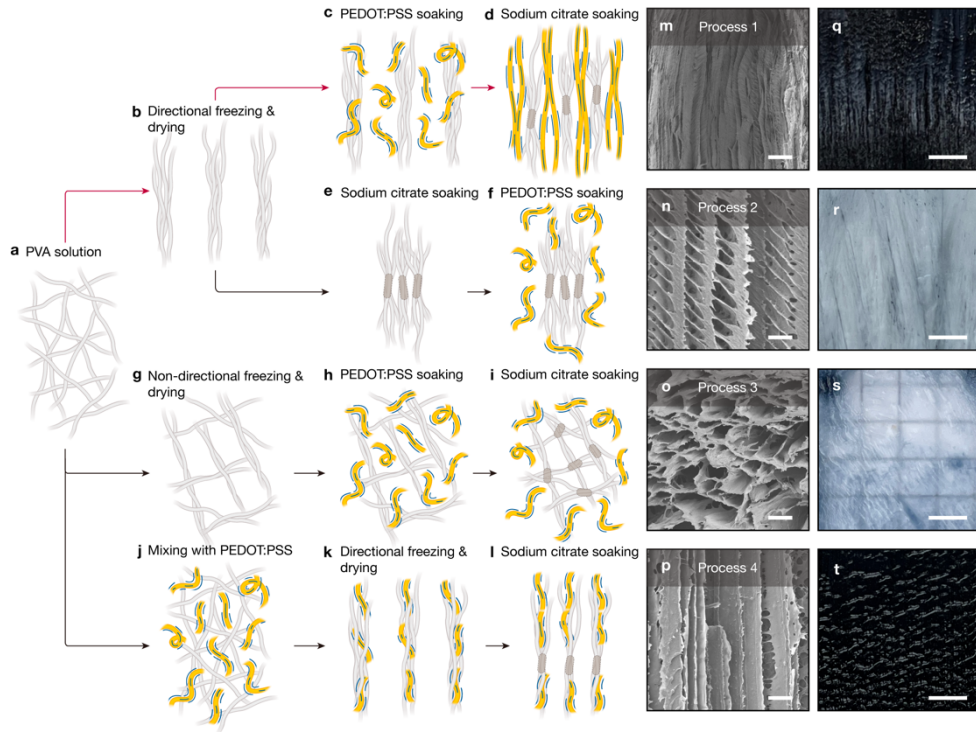


Figure 2.5 Effects of fabrication-process on microstructures.

(a–l) Schematic illustration of different fabrication-processes. (a, b, c, d) Process 1; (a, b, e, f) Process 2; (a, g, h, i) Process 3; (a, j, k, l) process 4. (m–t) Scanning electron micrographs (SEM) and (q–t) photographs depending on fabrication-process.

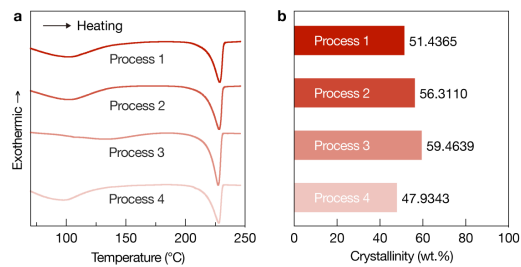


Figure 2.6 DSC profiles depending on fabrication-process. (a) DSC traces from first heating ramp. (b) The higher heat of melting measured by DSC, the higher the crystallinity.

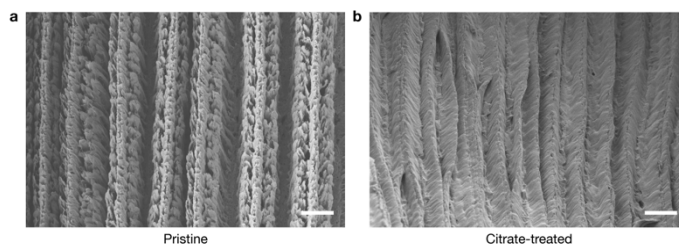


Figure 2.7 SEM images that show directionally aligned porous, pure PVA.

(a) pour PVA before sodium citrate treatment. (b) Citrated-treated PVA. Scale bars indicate 10 μm .

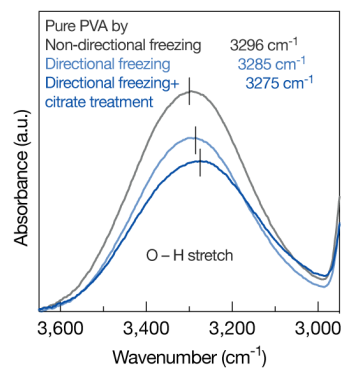


Figure 2.8 FTIR spectra of pure PVA dependent of freezing directionality and citrate treatment.

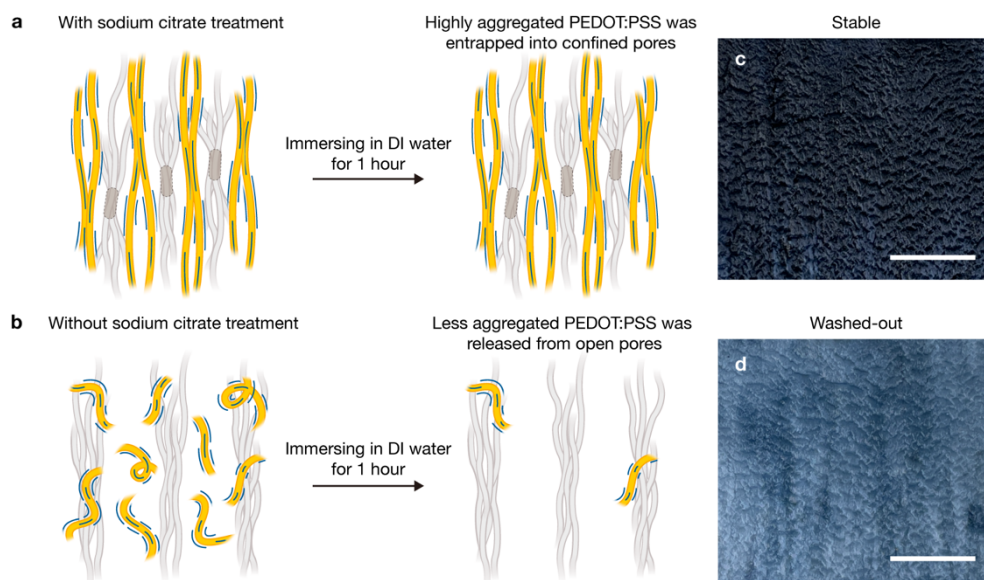


Figure 2.9 Washing tests for PEDOT:PSS aggregation by sodium citrate treatment.

PVA-PEDOT:PSS was washed with DI water after citrate treatment (a) and without citrate treatment (b). c,d Photographs of the washed PEDOT:PSS-PVA with citrate treatment (c) and without citrate treatment (d).

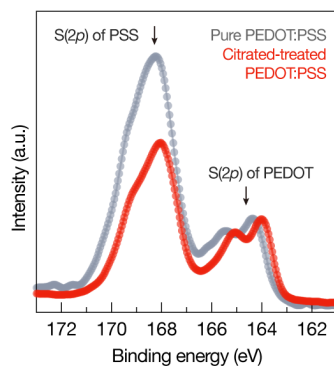


Figure 2.10 X-ray S 2p photoelectron spectra of pure PEDOT:PSS dependent of citrate treatment.

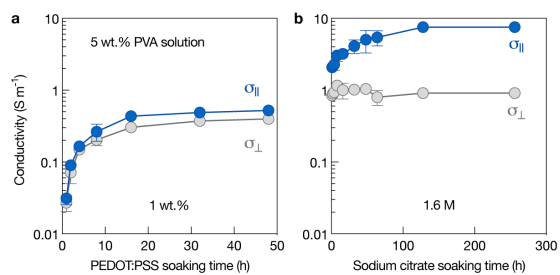


Figure 2.11 Soaking time effects for anisotropic conductivity.

(a) Conductivities were measured in the direction parallel (σ_{\parallel}) and perpendicular (σ_{\perp}) to the alignment direction as a function of PEDOT:PSS soaking time. (b) After finishing PEDOT:PSS infiltration for 48 h, the gels were transferred into a sodium citrate solution to align PEDOT:PSS. The conductivities were measured as a function of sodium citrate soaking time.

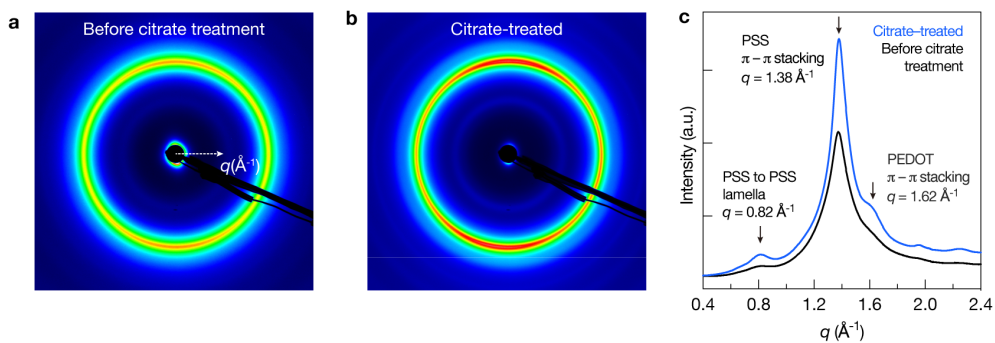


Figure 2.12 WAXS for PVA-PEDOT:PSS dependent of citrate treatment.

Two- dimensional WAXS patterns (a,b) and one-dimensional WAXS profiles (c) from azimuthal angle integration of the 2D WAXS data for PVA-PEDOT:PSS dependent of citrate treatment.

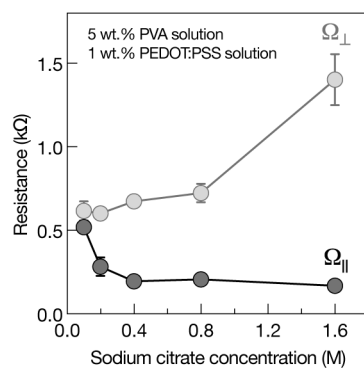


Figure 2.13 Parallel and perpendicular resistance of PVA-PEDOT:PSS as a function of sodium citrate concentration.

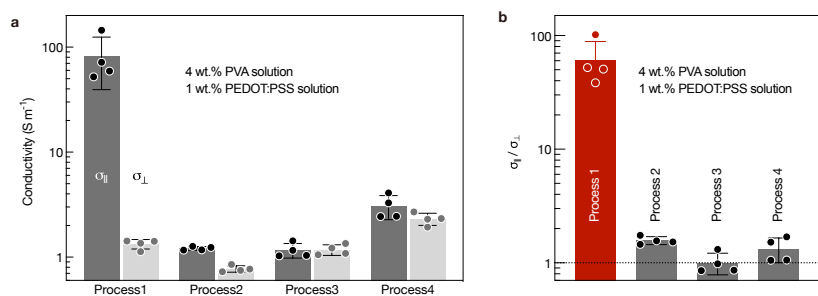


Figure 2.14 Effects of fabrication-process on anisotropic conductivity.

(a) Conductivity parallel and perpendicular to the alignment direction. (b) Conductivity ratio.

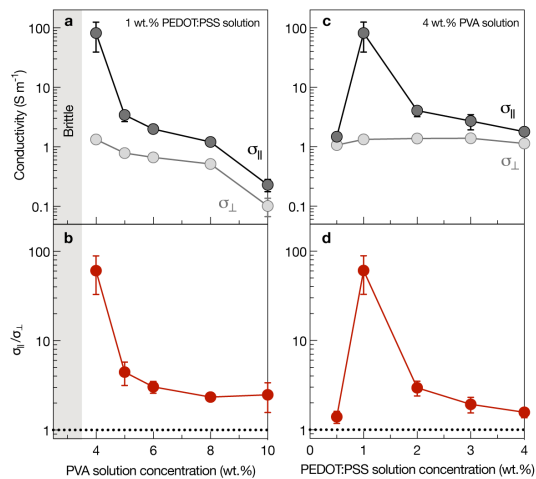


Figure 2.15 Effects of compositions on anisotropic conductivity.

(a–d) Conductivity and their ratio of PVA-PEDOT:PSS as a function of PVA concentration and PEDOT:PSS concentration.

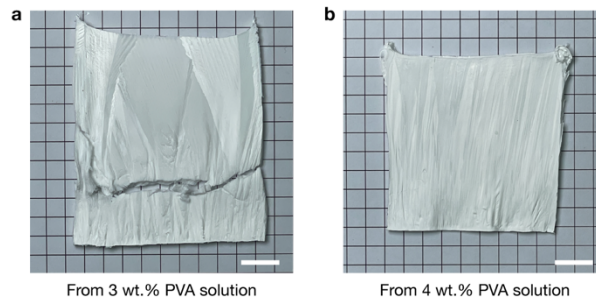


Figure 2.16 Aligned porous, pure PVA with directional freezing.

(a) from 3 wt.% PVA solution (b) from 4 wt.% PVA solution.

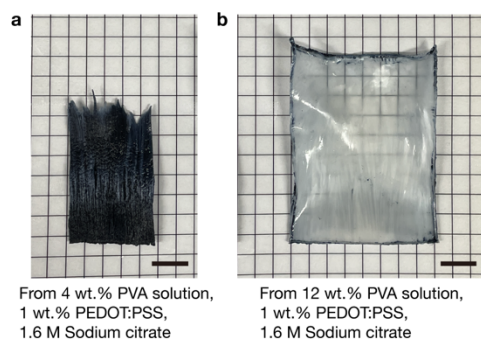


Figure 2.17 Apparency depending on PVA concentration.

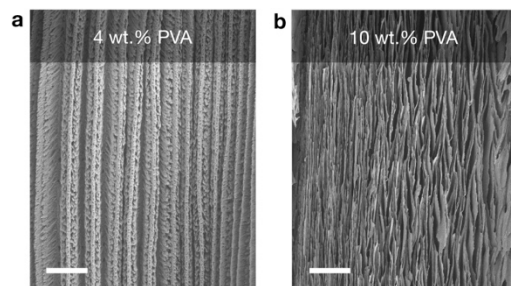


Figure 2.18 SEM images of pure PVA.

SEM images of pure PVA matrix from (a) 4wt.% and (b) 10 wt.% PVA solution.

Scale bar, 30 μm .

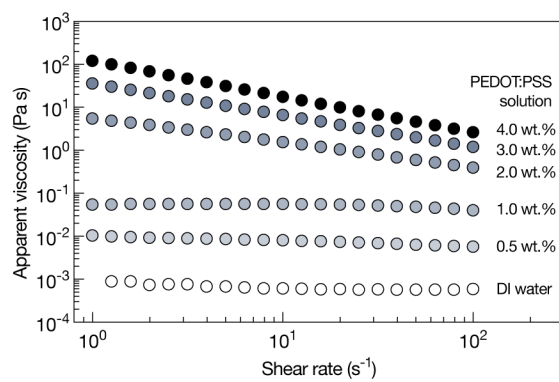


Figure 2.19 Apparent viscosity of pure PEDOT:PSS.

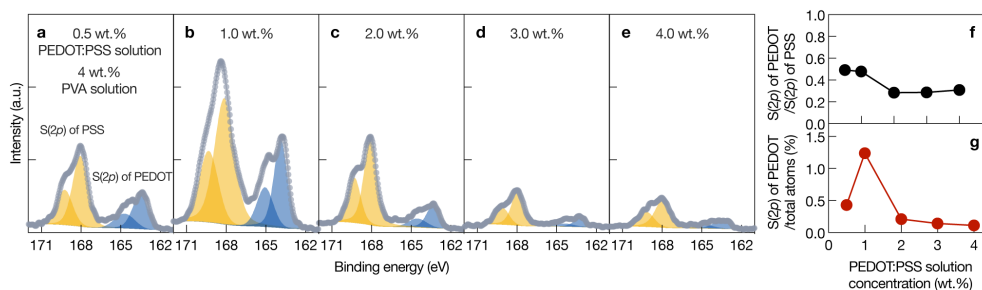


Figure 2.20 X-ray photoelectrons spectroscopy (XPS) S 2p spectra for PVA-PEDOT:PSS.

(a–e) X-ray photoelectrons spectroscopy (XPS) S 2p spectra for PVA-PEDOT:PSS.

The deconvoluted profiles were fitted with Gaussian-Lorentzian functions representing sulfur atoms from styrene sulfonate, SS (shades of yellow) and 3,4-ethylenedioxythiophene, EDOT (shades of blue). (f) Relative amount of sulfur atom of PEDOT to sulfur atom of PSS. (g) Amount of sulfur atoms of PEDOT to total atoms for PVA-PEDOT:PSS.

2.4 Conclusion

In hydrogel bioelectronics, the hydrogels form interfaces not only with the biological tissues but also with the electronic systems, typically in the form of metallic electrodes, interconnects, and external terminals. Together with hydrogel–tissue interfaces, hydrogel-device interfaces also play a critical role to achieve desirable bioelectronic performances and functionalities. However, conventional hydrogels have isotropic structure, thereby the hydrogels exhibit isotropic conduction with losing of electrical signal, thereby a highly electrically anisotropic conductive hydrogels based on controlled microstructure evolution can be utilized for a variety of biomedical applications such as epidermal sensors and implantable devices.

Chapter 3. Enhanced mechanical properties of hydrogels

3.1 Introduction

Engineering hydrogels are crosslinked polymer networks, wherein the hydrophilic polymer backbone enables swelling behavior capable of absorbing or retaining high water content. Their biophysical analogy to biological materials, such as extracellular matrix (ECM) ¹ or mucus ², and biocompatibility ³ make them compatible with biological systems. For example, they are broadly applicable to various fields, including artificial vascular networks ⁴, tissue replacements ⁵, epidermal sensors ⁶, and artificial muscle ⁷. However, their mechanical behaviors are incompatible with certain organ systems. For example, human skin exhibits both high stiffness (up to 100 MPa) ⁸ and toughness (up to 3,600 J m⁻²) ⁹ despite its high-water content (40–70 wt.%) ¹⁰, whereas existing hydrogels have rarely possessed both high stiffness and toughness. This is because compliant hydrogels usually become brittle when excess crosslinker is added to make the gel stiff. Furthermore, conventional hydrogels usually swell under physiological conditions and behave soft and compliant, weakening their mechanical properties. This swelling behavior also can limit their applicability for biomedical applications. For example, uncontrollable swelling may put pressure on nerve roots or damage to adjacent tissues from the installation sites ¹¹. To address the challenges associated with swelling and mechanical behaviors such as stiffness and toughness, various strategies have been contrived. One strategy lies in suppression of swelling. A non-swellaable hydrogel was achieved by the mixing of hydrophilic and thermo-responsive polymers, by which the opposing effects of swelling and shrinking render the gel non-swellaable,

even under physiological conditions¹². Another strategy is mechanical performance enhancement through material-hybridization. A hydrogel-composite was devised to exhibit high stiffness (up to 440 MPa) via calcification of calcium phosphate but has low toughness $< 1,000 \text{ J m}^{-2}$ ¹³. Alternatively, remarkable advances of toughness performance have been achieved by forming interpenetrating polymer network (IPN), wherein one network is brittle, and the other network is ductile. The brittle networks are used as sacrificial networks to dissipate energy, and the ductile networks maintain the shape during a deformation. Double-network (DN) hydrogel containing two covalently crosslinked networks was reported by J. P. Gong and her colleagues¹⁴. When DN gel is stretched, dense covalent crosslinks break and dissipate energy, exhibiting a fracture energy of $1,000 \text{ J m}^{-2}$. Another hydrogel with two ionic crosslinks was reported to exhibit a fracture energy of $4,000 \text{ J m}^{-2}$ via energy. Dissipation by rupturing weak ionic crosslinks, and strong ionic crosslinks maintain the shape of the gel¹⁵. While these are great advancements, in studies along these lines, the gels do not possess both high stiffness and toughness at the same time.

Another hydrogel with an extreme fracture toughness of $9,000 \text{ J m}^{-2}$ was achieved by introducing reversible ionic crosslinks into covalent crosslinks. Upon stretching, the covalently crosslinked networks bridge cracks and stabilize the deformation and energy dissipation by unzipping ionic crosslinks reduces stress concentrations.¹⁶. The ionic crosslinks density of the alginate gels can be modulated with multivalent cations. Specifically, alginate gels with trivalent Fe^{3+} and Al^{3+} cations exhibit higher stiffness than those with divalent cations¹⁷. Moreover, the proved biocompatibility of alginate gels enables their use in diverse biomedical applications, such as wound dressings, pharmaceuticals, cell culture, and tissue regeneration¹⁸. The conventional method of injecting high concentrations of Fe^{3+} ions directly into the gel has a

limitation of creating a non-uniform hydrogel that has many ionic bonds only in the local area. Thus, ions were slowly infiltrated by diffusion by soaking in a high concentration of Fe^{3+} ions solution, and almost all parts of the alginate chain were ionically crosslinked to improve stability.

In this study, we designed a non-swelling hydrogel by building up IPN between covalently crosslinked pHEMA and ionically crosslinked alginate. The stiffness is enhanced by utilizing ionic crosslinking sites fully, and toughness is enhanced by adopting synergistic effects between energy dissipation by ionic networks and crack bridging by covalent networks. Non-swelling behaviors of the gel are achieved by densifying covalent and ionic crosslinks. Cytotoxicity is also evaluated to assess applicability of the gel to biomaterials.

3.2 Experimental section

3.2.1 Gel preparation

pHEMA-alginate interpenetrating network (IPN) gels were prepared by mixing alginate and HEMA in deionized water. The water concentration ($\frac{\text{water wt}}{(\text{HEMA} + \text{alginate} + \text{water}) \text{ wt}} \times 100$) was fixed at 55wt.% throughout the experiments for the IPN, and the polymer ratios were varied by mixing different amounts of HEMA and alginate. MBAA 0.333 wt.% and APS 0.1 wt.% with respect to the weight of the HEMA monomer were added as covalent crosslinking agents and a redox radical initiator, respectively. After degassing in a vacuum chamber, TEMED 0.34 wt.% with respect to the weight of the HEMA monomer were added as an accelerator. Under redox radical polymerization, oxygen acts as a quencher of the excited states of the molecules and thereby inhibits polymerization. This issue was

addressed by performing the polymerization under an isolated glass mold system. The solutions were poured into a $100.0 \times 100.0 \times 2.0 \text{ mm}^3$ glass mold and covered with a 5-mm-thick transparent glass plate. For reaction activation, the gels were cured by ultraviolet irradiation (UVC, CL-1000L) for 4 h with 8 W power and a 365 nm wavelength at room temperature. The gels were then kept in moist storage for 1 day to stabilize the reactions before ionic crosslinking.

The covalently crosslinked gels were steeped in the prepared iron (III) nitrate nonahydrate solutions at various molar concentrations (1 mol L^{-1} , 2 mol L^{-1} , 3 mol L^{-1} and 5 mol L^{-1}) at room temperature. At designated time points, the gels were taken out and washed with fresh deionized water to remove excess ions on the surface of the gels. The gels were then kept in moist storage for 24 h to stabilize the ionic crosslinking.

3.2.2 Tensile test preparation

Before the mechanical tests, the surfaces of the hydrogels were dried with N_2 gas for 1 min to remove water from the gel surfaces. Tensile specimens were cut into a dumbbell configuration with two enlarged shoulders and a reduced gauge section (standard: DIN 53504, type: S3a) using a laser cutter (Universal Laser System, VLS 3.50). Four stiff acrylic plates were glued with superglue (3 M) to clamp the gel. Test specimens were prepared to a standard size (50 mm in overall length, 8.5 mm in shoulder width, 4 mm in narrow width, 2 mm in thickness and 10 mm in gauge length). The specimens were mounted into the holding grips of a universal testing machine (Instron, 3343) with a 50 N capacity load cell. All mechanical tests were performed at room temperature. Tensile test outputs were recorded as nominal stress and stretch. The strain rate was kept constant at $= 3 \text{ min}^{-1}$.

3.2.3 Fracture test preparation

Fracture test specimens were prepared at 20.0 (width) \times 40.0 (length) \times 2.0 (thickness) mm³ using a laser cutter. For notched specimens, notches 10 mm in length were made using a razor blade with an initial notch size $C_0/L \approx 0.5$, where C_0 is initial notch length and L is width of the specimen. To prevent slippage between jaw faces and specimens, 60 grit silicon carbide paper (Allied High Tech Products, Inc.) was bonded with superglue to jaw faces in the tensile machine. The specimens were mounted into 4 holding grips with 5-mm-initial distances (L_0) between the upper and lower jaw faces. During uniaxial stretching, crack propagation was monitored by a camera to record critical distance (L_c) between the upper and lower jaw faces at crack onset propagation. Images were captured at a rate of 60 frames/s. The strain rate was kept constant at $= 3 \text{ min}^{-1}$.

3.2.4 *in vitro* swelling test

To investigate the *in vitro* swelling behaviors, covalently cross-linked gels in step 1 were prepared in disc-shaped samples with initial volume (V_0) at a diameter and thickness of 10 mm and 2 mm, respectively. The gels were soaked in Fe^{3+} solutions for ionic crosslinking at room temperature. In step 2, gel volumes (V_{Fe}) were measured at designated time points of 0.083, 0.16, 0.25, 0.3, 0.416, 1, 2, 3, 4, 8, 16 and 32 h. The step 1 gels taken out of the $\text{Fe}(\text{NO}_3)_3$ solution were washed 3 times with deionized water to remove excess ions on surface of the gels, and transferred to Dulbecco's Phosphate Buffered Saline (DPBS) solutions kept at room temperature. DPBS solutions (1 \times) were prepared by tenfold diluting of DPBS (10 \times). The volumes (V_{DPBS}) of the ion-released gels were recorded as a function of soaking time in DPBS

3.2.5 *in vivo* swelling test

For *in vivo* swelling tests, hybrid hydrogels were prepared and sterilized with ethylene oxide gas. Each hybrid hydrogel was prewetted in PBS for 2h. The hybrid hydrogels were implanted into the sub-cutaneous dorsum of 7-week-old male Sprague-Dawley rats (Nara Biotech, Korea). Rats were sacrificed at 7 or 21 days ($n = 3$). All animal protocols followed the regulations of the committee on the safety and ethical handling of laboratory experiments of the Korea Institute of Science and Technology and were in accordance with the recommendations for handling of laboratory animals for biomedical research (2014-06068).

3.2.6 Live/dead staining

To evaluate cell viability in a gel conditioned medium, various hydrogels were prepared and sterilized with ethylene oxide gas. Human bone marrow mesenchymal stem cells (hBMSCs, Lonza, Switzerland) were purchased and cultured in Dulbecco's modified Eagle's medium/ high glucose medium supplemented with 10% fetal bovine serum and 1% penicillin/streptomycin in a humidified atmosphere under 5% CO₂. To prepare the gel conditioned medium, individual hydrogels were placed in conical tubes containing culture medium and incubated for various time points (3, 7, 14, 30, or 60 days) at 37 °C and 5% CO₂. The hBMSCs (P5) were seeded at 1×10^4 cells/well and cultured in 24-well plates for 1 day in culture conditions. After cell adhesion, the culture media were removed and switched to gel conditioned media (500 μ L/ well). After 24 h, the cells were washed with $1 \times$ PBS, and a cocktail of ethidium homodimer-1 (EthD-1) and calcein acetoxymethyl (AM) was added to each well. Live/Dead Kits (Thermo Fisher Scientific, USA) were used. After a 30-minute incubation at room temperature, the labeled cells were observed by

fluorescence microscopy (Eclipse TE2000U). For the quantitative analysis of cell viability, the images of all groups were taken in three random fields at 100× magnification with a blinded rater in border zones (n = 3 in each group).

3.3 Results and Discussion

3.3.1 Fabrication

Poly(2-hydroxyethyl methacrylate) (pHEMA) is used as a covalently crosslinked polymer network. pHEMA exhibits less swelling behavior despite its hydrophilicity^{19,20}, having approximately 40 wt.% equilibrium water content²¹. Moreover, pHEMA is a proved biocompatible polymer²², which can be used in such biomedical applications as artificial corneas²³, scaffolds²⁴, drug delivery devices²⁵, and nerve guidance channels²⁶. However, single network hydrogels made from pHEMA are soft and brittle. We addressed these challenges by introducing energy-dissipating mechanism wherein the unzipping of ionically crosslinked networks reduces stress concentrations of covalently crosslinked pHEMA networks. Here, alginate is used as ionically crosslinked polymer. Alginate, a polysaccharide composed of mannuronic acids (M units) and guluronic acids (G units), are built up by blocks of consecutive M units (M-blocks), consecutive G units (G-blocks), and alternating M and G units (MG-blocks). In a solution, the G blocks form ionic crosslinks with multivalent cations, resulting in the formation of hydrogels.

We fabricated a pHEMA-alginate hybrid gel via a stepwise process as shown in Fig. 3.1. A hybrid hydrogel was obtained by the stepwise crosslinking of two different polymer systems. In the first step (Fig. 3.1 a), pHEMA networks (gray dotted line) were produced by covalent cross- linking (MBAA, blue square) via

radical polymerization. Ammonium persulfate (APS)/N,N,N',N'-tetramethylethylenediamine (TEMED) was used as a redox initiator ²⁷. However, under radical polymerization, oxygen acts as a quencher of the excited state of the molecules and thereby, inhibits polymerization. This issue was addressed by performing the polymerization under an isolated glass mold system. In the second step (Fig. 3.1 b), the gel prepared in the first step after covalent crosslinking was soaked in an iron (III) nitrate solution at room temperature. Fe³⁺ ions (yellow circle) permeated into the gel (yellow solid arrows denote the permeation direction of Fe³⁺ ions). Simultaneously, alginate chains (black solid line) were ionically crosslinked as the Fe³⁺ ions moved toward ionic crosslinking sites (yellow dotted circles). We adopted this soaking method because iron (III) nitrate salts have higher solubility than the chloride or sulfate salts. A higher solubility enables the full ionic crosslinking of alginate chains. Furthermore, higher solubility produces non-homogeneous hydrogels due to drastically different ionic crosslinking rates. The resultant product formed interpenetrating polymer networks (IPNs) between the MBAA-crosslinked pHEMA network and the Fe³⁺-crosslinked alginate network. In the final step (Fig. 3.1 c), the prepared gel was transferred to Dulbecco's Phosphate-Buffered Saline (DPBS) to wash out unreacted Fe³⁺ ions remaining within the pHEMA-alginate hybrid hydrogel. Any residual Fe³⁺ would otherwise have physiological side effects ²⁸. The green dotted arrows indicate the release direction of Fe³⁺ ions. We compared the pHEMA-alginate hybrid hydrogels (92.31 wt.% HEMA/(HEMA + alginate), 0.333 wt.% MBAA/HEMA, and 5 mol L⁻¹ Fe(NO₃)₃ soaking solutions for 16 h) during the different reaction steps. The gel prepared in step 1 after covalent crosslinking exhibits a soft and opaque appearance (Fig. 3.2 a and Fig. 3.3 a). However, the gels prepared in steps 2 and 3 after ionic crosslinking

exhibit stiff and golden semi-transparent, irrespective of washing and swelling in DBPS (Fig. 3.2 b,c and Fig. 3.3 b,c).

3.3.3 Hybrid gels

We further compared the pHEMA-alginate hybrid hydrogel (55.0 wt.% water content, 92.31 wt.% HEMA/(HEMA + alginate), 0.333 wt.% MBAA/HEMA, and 5 mol L⁻¹ soaking solution for 16 h) with pHEMA gel (70.8 wt.% water content, 0.333 wt.% MBAA/HEMA) and alginate gel (96.7 wt.% water content, 5 mol L⁻¹ soaking solution for 16 h) with respect to mechanical behaviors. The amounts of HEMA and alginate in the hybrid gel were kept the same as those in the pHEMA gel and alginate gel, respectively. The gels were shaped into a tensile test specimen using a laser cutter with dumbbell configuration (DIN 53504; Fig. 3.4). The gel samples were subjected to a uniaxial tensile test to determine its rupture point with a universal testing machine (Instron, 3343) using a 50 N load cell. The stretch is defined according to $\lambda = (l_0 + \Delta l)/l_0$, where l_0 is the original non-deformed gauge length, and Δl is the change in length at some instance in time. The rate of stretching was constant at = 3 min⁻¹. In stress-stretch curves (Fig.3.5), the hybrid hydrogel exhibits superior mechanical properties with elastic modulus of 48.21 MPa which is 29 and 210 times higher than those of the alginate gel and the pHEMA gel, respectively.

3.3.3 Stiffness and toughness

We demonstrated high stiffness and toughness via a pre-cracked hybrid hydrogel (92.31 wt.% HEMA/(HEMA + alginate), 0.333 wt.% MBAA/HEMA, and 5 mol L⁻¹ soaking solution for 16 h) with 20 mm² cross-section; width, pre-crack length, and thickness of 20 mm, 10 mm, and 2 mm, respectively (Fig. 3.6). The pre-cracked

hybrid gel sustains a large load of 2 kgf without crack propagation under a small deformation of $\lambda = 1.2$. These data imply that the integrated stiffening and toughening mechanisms enhanced the mechanical performance of the gels.

Fracture tests as introduced by Rivlin and Thomas were implemented to measure fracture energies (Γ) of the hybrid gels with various polymer ratios (Details about the fracture tests were described in Fig. 3.10 a-c) ³⁰. A 10-mm notch was made in rectangular gels with 20-mm width using a razor blade with an initial notch size $C_0/L \approx 0.5$, where C_0 is the initial notch length and L is width of the gel. The notched gels were uniaxially stretched. When critical distances (h_c) were reached, the pre-crack became a running crack and began to propagate toward the edge. The critical stretch (λ_c) is defined as the critical distance (h_c) divided by the initial distance between the upper and lower jaw face (h_0). The fracture energy (Γ) was calculated by using the following equation³⁰ where t represents a thickness of an un-deformed gel, and $U(h_c)$ is the area under the force-distance curves from zero to critical distance. Critical stretches (black line) and fracture energies (blue line) were plotted against various weight ratios in Fig. 3.11. The maximum fracture energy of the hybrid gel was 8850 J m^{-2} at 90.91 wt.%. pHEMA-alginate hybrid gel exhibits high stiffness and toughness as signified by high elastic moduli of approximately 108 MPa and by high fracture energies of approximately 8850 J m^{-2} . This performance is nearly consistent with human skin, and better than those of the state-of-the-art synthetic hydrogels, such as p(Nass-co-MPTC) gel ¹⁵, AAm-alginate gel¹⁶, and calcification-induced gel ¹³ (Fig. 3.12).

3.3.4 Fe³⁺ ionic crosslinking density effect

Crosslinking between polymer chains results in different lengths depending on the

crosslinking method employed and specific conditions. Specifically, higher degrees of crosslinking render high stiffness and non-swellability in physiological conditions²⁹. We examined crosslinking density effects by modulating the Fe^{3+} concentrations of soaking solution, soaking times, and MBAA/HEMA weight ratios (Fig. 3.7 a). To examine the ionic crosslinks density effects, the covalently crosslinked gels in step 1 were prepared with a 94.12 wt % HEMA/(HEMA + alginate) ratio and a 0.333 wt.% MBAA/HEMA ratio. The gels were soaked at different molar concentrations (1 mol L^{-1} , 2 mol L^{-1} , 3 mol L^{-1} and 5 mol L^{-1}) of iron(III) nitrate nonahydrate solutions. After ionic crosslinking for 16 h, stress-stretch curves were obtained by stretching tensile specimens to rupture (Fig. 3.7 a–c). Experiments performed at fixed Fe^{3+} concentrations revealed soaking time effects (Fig. 3.7 b). The gels prepared in step 1 were soaked in 5 mol L^{-1} concentration of $\text{Fe}(\text{NO}_3)_3$ solution. The soaked gels were removed at designated ionic crosslinking times of 30 min, 1 h, 2 h, 4 h, 8 h and 16 h, and stress-stretch curves were obtained by stretching tensile specimens to rupture. Elastic moduli were determined from the stress-stretch curves by varying the Fe^{3+} concentrations of the soaking solutions and the soaking time, and were plotted as a function of soaking times (Fig. 3.7 c). After starting a soaking, the elastic modulus linearly increased over a period of 8 h. Thereafter, the elastic modulus increased more slowly and eventually reached a maximum value at 16 h, which suggests a minimum time for full ionic crosslinking.

3.3.5 Covalent crosslinking density effect

In addition to ionic crosslinks density, covalent crosslinks density also affects mechanical properties. Hybrid gels with various weight ratios of MBAA/HEMA and fixed HEMA/(HEMA + alginate) ratios, soaking solution Fe^{3+} concentrations, and

soaking times (90.91 wt.%, 5 mol L⁻¹, and 8 h, respectively) were prepared and subjected to tensile tests. The resultant stress-stretch plots were shown in Fig. 3.8 a. The elastic modulus was plotted as a function of the MBAA/HEMA weight ratio in Fig. 3.8 b. The elastic modulus initially increased with an increasing MBAA/ HEMA ratio and reached a maximum of 69.45 MPa at 0.2 wt.% and subsequently decreased at higher ratios.

3.3.6 Polymer ratio effect

We further demonstrated that by tuning the polymer ratios of HEMA/alginate, hybrid gels can be engineered with enhanced mechanical properties. Hybrid gels with various weight ratios of HEMA/ (HEMA + alginate) were subjected to tensile tests to characterize their mechanical properties (Fig. 3.9 a). The elastic modulus was plotted as a function of the weight ratios of HEMA/(HEMA + alginate) in Fig. 3.9 b. The major increase in stiffness occurred between 90.91 and 94.74 wt.%, when elastic modulus increased from 3.11 to 74.98 MPa, with only a slight increase in weight ratios of alginate from 5.26 to 9.09 wt.%. The minor increase at 90.91wt.% indicates that the elastic modulus increased slowly above 90.91wt.% and reached a maximum value of 108 MPa at 85.71 wt.%.

3.3.7 *in vitro* swelling test

Generally, hydrogels swell under aqueous conditions, with drastically altered mechanical properties dependent on the degree of swelling. We estimated *in vitro* and *in vivo* swelling behaviors (Fig. 3.14). In DPBS, swelling was investigated under physiological *in vitro* conditions (Fig. 3.14 a,b). DPBS provides a sufficient physiological environment with respect to body ion concentrations³¹. Covalently

crosslinked gels in step 1 (92.31 wt.% HEMA/(HEMA + alginate), 0.333 wt.% MBAA/ HEMA) were prepared in disc-shaped samples with an initial volume (V_0) and diameter and thickness of 10 mm and 2 mm, respectively. In step 2, the gels were soaked in 5 mol L⁻¹ Fe(NO₃)₃ solution. Fe³⁺ ions penetrated into the gel to ionically crosslink alginate chains. Gel volumes (V_{Fe}) were measured as a function of Fe(NO₃)₃ solution soaking time and swelling ratios (V_{Fe}/V_0) were plotted (Fig. 3.14 a, left black line). The gels drastically de-swelled up to 0.1h and reached equilibrium swollen states after 3 h. The gels were transferred to DBPS after full ionic crosslinking of 32 h. Unreacted Fe³⁺ ions were removed in step 3, and the volumes (V_{DBPS}) of the gels were measured as a function of DPBS soaking time (Fig. 3.14 a, right blue line). The swelling ratio (V_{DBPS}/V_0) was constant regardless of the DPBS soaking time. We performed tensile tests at designated swelling times in DPBS (Fig. 3.15). The elastic modulus was constant regardless of the DPBS soaking time. These results indicated that swelling did not break the covalent or ionic cross- links, showing that the hybrid gels had non-swellability under physiological conditions without losses in mechanical properties.

3.3.8 *in vivo* swelling test

In vivo swelling behaviors were monitored via hydrogel implantation in rats (Fig. 3.16 a,b). Hybrid hydrogels (92.31wt.% HEMA/ (HEMA + alginate) and 0.333 wt.% MBAA/HEMA) prepared in 5 mol L⁻¹ soaking solutions for 16 h were cut into a disc shape using a laser cutter, with an initial volume (V_0) corresponding to 10mm in diameter and 2 mm in thickness. Before implantation in rats, the gels were sterilized with ethylene oxide gas and pre-wetted in PBS for 2 h. The hybrid hydrogels were implanted into the subcutaneous dorsum of 7-week-old male Sprague-Dawley rats

(Fig. 3.16 a). The gels implanted in vivo were explanted after day 7 or 21. The volumes of the explanted gels were measured and plotted as a function of in vivo implantation time (Fig. 3.16 b). The swelling ratio ($V_{\text{in vivo}}/V_0$) was constant regardless of the in vivo implantation time. The in vivo results coincided with the observed in vitro swelling behaviors.

3.3.9 Cytotoxicity test

To experimentally validate whether the hybrid gels had potential cytotoxicity for biomedical applications, cell viability assays were conducted using gel-conditioned media (Fig. 3.17). Alginate gel, pHEMA gel, non-ionically crosslinked hybrid gel, and hybrid gels soaked in $\text{Fe}(\text{NO}_3)_3$ soaking solutions at 1 mol L^{-1} , 2 mol L^{-1} , 3 mol L^{-1} and 5 mol L^{-1} were prepared, and sterilized with ethylene oxide gas. The gels were incubated in culture media. At time points of 3, 7, 14, 30 and 60 days, human bone marrow mesenchymal stem cells (hBMSCs) were cultured in each gel-conditioned medium for 1 day. Live/dead staining assays were used to visually assess cell viability. Fluorescence imaging of cells revealed that the hybrid gels showed no significant differences in cell viability when compared with control and either alginate or pHEMA gel (Fig. 3.18). Moreover, high cell viability was observed after 60 days. These results suggest that the hybrid gels are cytocompatible.

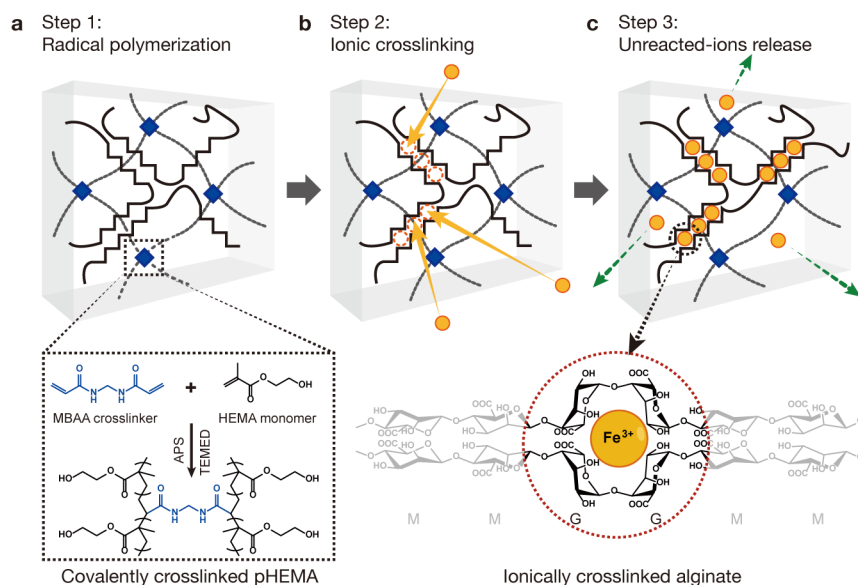


Figure 3.1 The hybrid hydrogels are obtained by the stepwise crosslinking of two different polymer systems.

(a) In the first step, MBAA-crosslinked pHEMA networks were produced via radical polymerization. (b) In the second step, Ionic crosslinks were induced by soaking the gel in a $\text{Fe}(\text{NO}_3)_3$ aqueous solution, where Fe^{3+} ions (yellow solid circles) move to ionic crosslinking sites (yellow dotted circles). (c) In the final step, the unreacted Fe^{3+} ions were released (green dotted arrows) in DPBS.

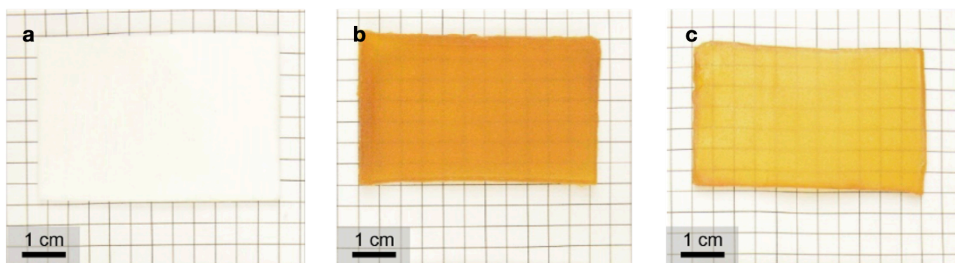


Figure 3.2 Images of pHEMA-alginate hydrogels in each step.

(a) after covalent crosslinking, (b) after ionic crosslinking, and (c) after unreacted-ion release.

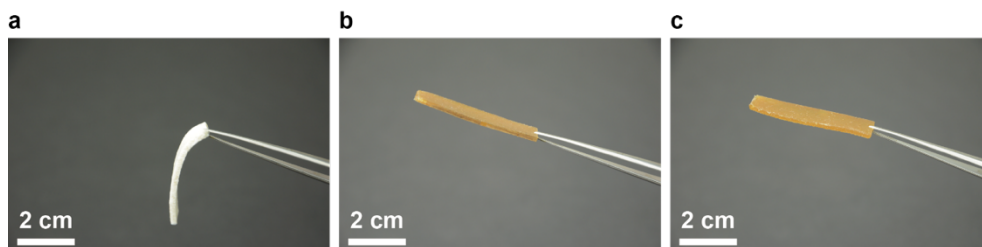


Figure 3.3 We compared the pHEMA-alginate hybrid hydrogels during the different reaction steps.

(a) The gel prepared in step 1 after covalent crosslinking exhibits a soft. (b,c) However, the gels prepared in steps 2 and 3 after ionic crosslinking exhibit stiff, irrespective of washing and swelling in DBPS.

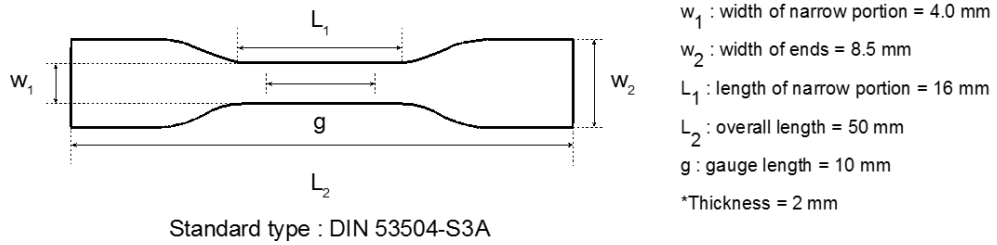


Figure 3.4 Tensile test specimen configuration.

We prepared all tensile test specimens using a laser cutter with dumbbell configuration.

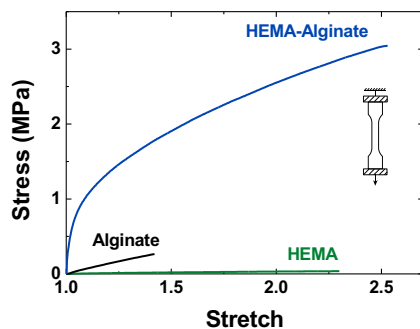


Figure 3.5 Comparison of pHEMA gel, alginate gel, and pHEMA-alginate gel in stress-stretch curves.

The gels were subjected to a controlled tension stretch to determine its rupture point with a universal testing machine (Instron, 3343) using a 50 N load cell. The amounts of HEMA and alginate in the hybrid gel were kept the same as those in the pHEMA gel and alginate gel, respectively. Water content was fixed at 55.0 wt.%, 96.7 wt.% and 70.8 wt.% for hybrid gel, alginate gel and pHEMA gel, respectively.

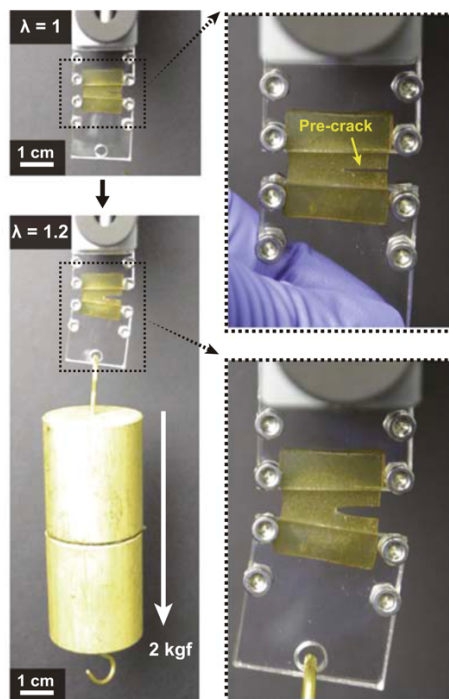


Figure 3.6 A demonstration of high stiffness and toughness for the pHEMA-alginate hydrogels.

A pre-cracked hybrid gel (2 mm-thick) can sustain a large load of 2 kgf without any crack propagation. Weight ratios between HEMA/(HEMA + alginate) and MBAA/HEMA were fixed as 92.31 wt.% and 0.33 wt.%, respectively. 5 mol L^{-1} $\text{Fe}(\text{NO}_3)_3$ solutions were used for 16 h in step 2.

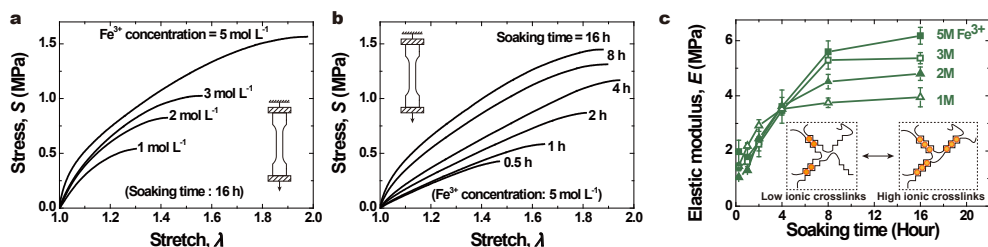


Figure 3.7 Ionic crosslinks effects.

(a) Stress-stretch curves with respect to the Fe^{3+} concentration in a soaking solution. Soaking time is 16 h. (b) Stress-stretch curves with respect to soaking times. 5 M $\text{Fe}(\text{NO}_3)_3$ aqueous solutions were used for the soaking. (c) Elastic moduli of the gels were investigated as a function of soaking time for various concentrations of soaking solutions.

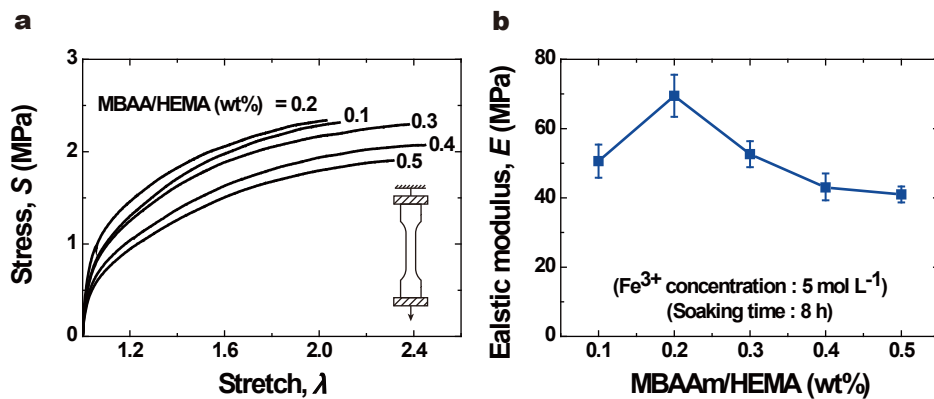


Figure 3.8 Covalent crosslinks effects.

(a) The effect of covalent crosslinker (MBAA) on stress-stretch curves is shown. (b)

Elastic modulus of the gel was not influenced by the concentration of MBAA to a significant degree.

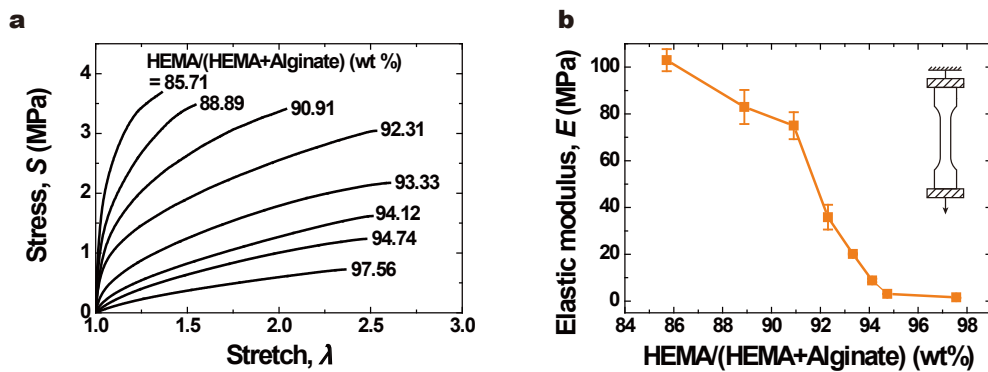


Figure 3.9 Polymer ratio effects.

(a) The hybrid gels with various weight ratios of HEMA/(HEMA + alginate) were stretched to rupture. (b) Elastic moduli calculated from the stress-stretch curves were plotted as a function of HEMA/(HEMA + alginate).

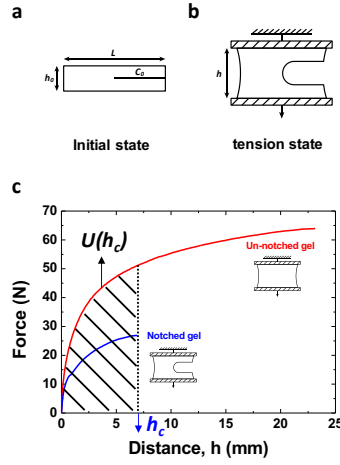


Figure 3.10 Fracture tests introduced by Rivlin and Thomas.

To measure fracture energy, we implemented fracture tests introduced by Rivlin and Thomas. (a) Notched gel was prepared with a width (L) of 20 mm, notch length (C_0) of 10 mm, and thickness (t) of 2 mm. The notched gel mounted into universal testing machine with initial distance (h_0) between upper and lower jaw face. (b) Upon the notched gel stretching, images were recorded by a camera at a rate of 60 frames/sec to capture a critical distance (h_c) between the upper and lower jaw face, when the notch became a running crack. (c) Un-notched gel was subjected to tension force in order to plot the force-distance curve. $U(h_c)$ is the area under the force-distance curve from zero to critical distance (h_c). The fracture energy was calculated by using the following equation, $\Gamma = U(h_c)/Lt \text{ J m}^{-2}$.

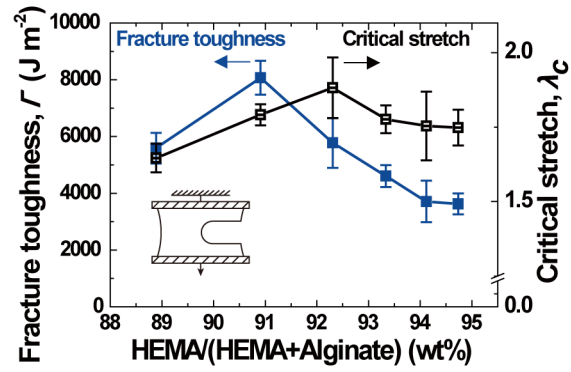


Figure 3.11 Fracture tests were performed with notched gels.

Fracture energy and critical stretch were plotted with various weight ratios of HEMA/(HEMA + alginate).

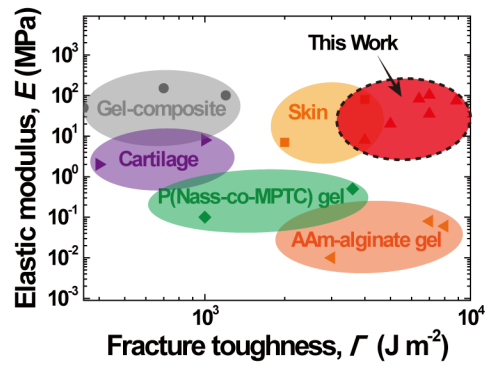


Figure 3.12 Elastic modulus versus fracture energy plots for a variety of materials.

p(Nass-co-MPTC) gel, AAm-alginate gel, and calcification-induced gel composites along with cartilage and skin were plotted.

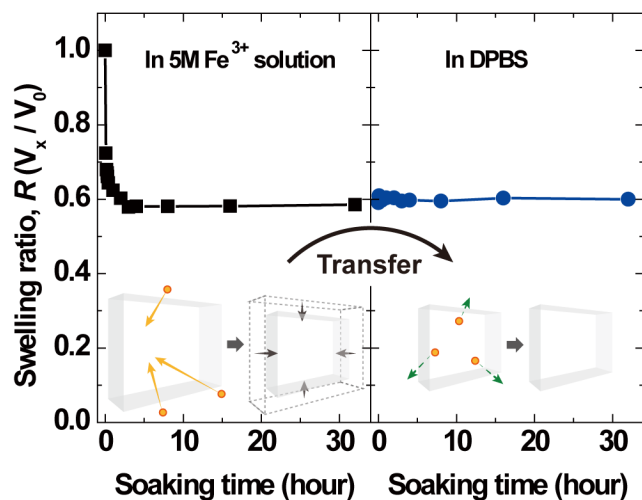


Figure 3.13 *in vitro* swelling behaviors.

(a, b) *In vitro* swelling behaviors were investigated under physiological conditions. After step 1 process, covalently crosslinked gels with initial volume (V_0) were soaked in $\text{Fe}(\text{NO}_3)_3$ aqueous solutions. The volume of the gel in $\text{Fe}(\text{NO}_3)_3$ solutions (V_{Fe}) was measured as a function of soaking time. After finishing ionic crosslinking for 32 h, the gels were transferred into a DPBS solution to release unreacted ions in the gels. The volumes (V_{DPBS}) of the gels were measured as a function of the DPBS soaking time.

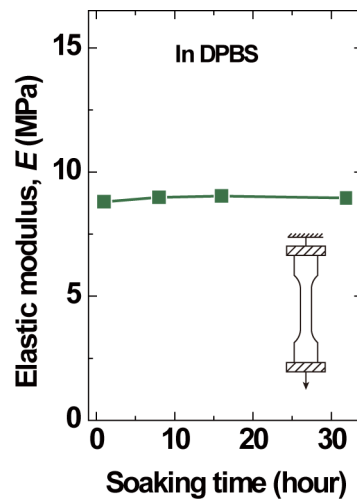


Figure 3.14 Elastic modulus of the gel was measured as a function of ion release time in a DPBS solution.

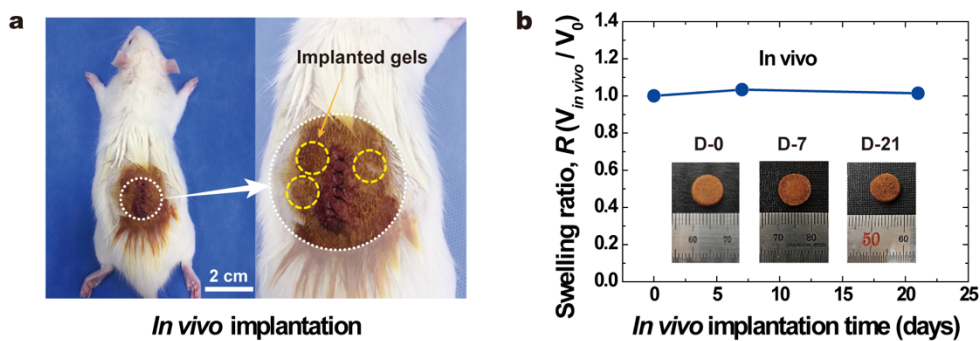


Figure 3.15 *in vivo* swelling behaviors were monitored via hydrogel implantation in rats.

(a) Disc-shaped hybrid gels with a diameter of 10 mm and a thickness of 2 mm were implanted into the subcutaneous dorsum. (b) The hybrid gel samples were explanted on days 7 and 21. Swelling ratios were measured. The error bars indicate the standard deviation of $n = 3$.

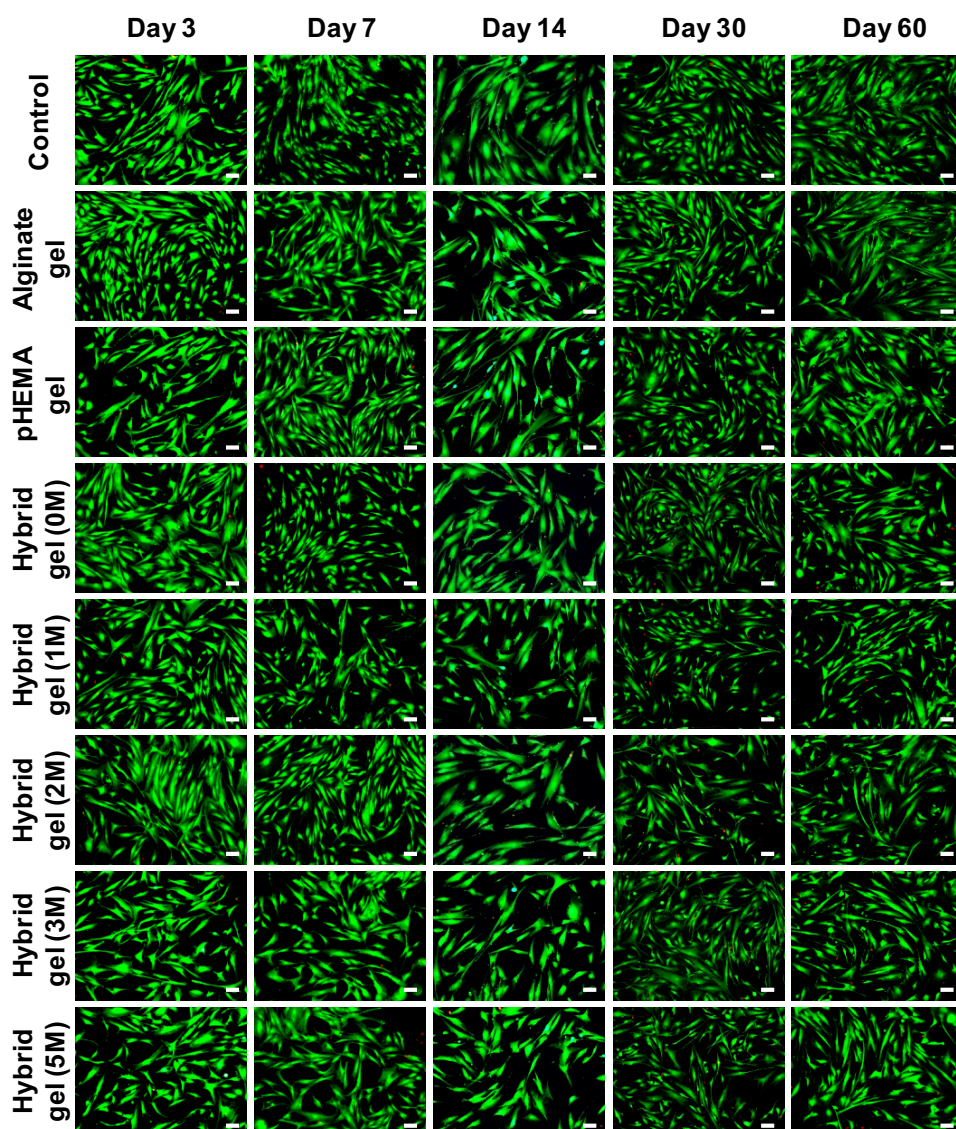


Figure 3.16 Evaluation of cell viability in gel-conditioned media.

The gel-conditioned media were prepared for an alginate gel, a pHEMA gel and hybrid gels. The hybrid gels were soaked in various concentrations of $\text{Fe}(\text{NO}_3)_3$ aqueous solutions (1, 2, 3, and 5 mol L^{-1}) for 16 hours. Individual hydrogels were incubated for various time points (3, 7, 14, 30 and 60 days). In the fluorescent images of cell cultures, live cells stain green and dead cells stain red. Scale bar, 200 μm .

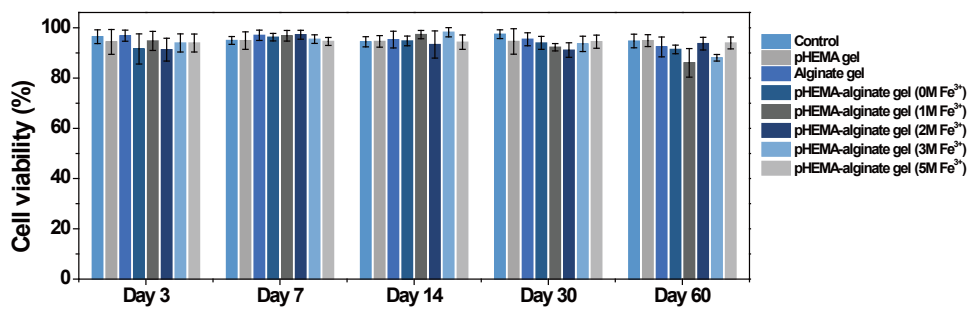


Figure 3.17 Cell viability percentage as a function of gel-conditioning times for a variety of gels.

The error bars indicate the standard deviation of $n = 3$.

3.4 Conclusion

In summary, we have overcome the challenge of integrating high stiffness and toughness with non-swelling into a hybrid gel by building up IPN between covalently crosslinked pHEMA networks and ionically crosslinked alginate networks. The stiff and tough behaviors of the hybrid gel are attributed to the integrate stiffening and toughening mechanisms. The stiffness is enhanced by utilizing ionic crosslinking sites fully via the soaking method, differing from other hydrogels in that they have a partial ionic crosslinks via in situ ionic crosslinking method, and toughness is enhanced by synergistic effects; energy dissipation by densely crosslinked ionic networks and strong crack bridging by densely crosslinked covalent crosslinks. The hybrid hydrogel exhibited high elastic moduli (up to 108 MPa) and high fracture energies (up to 8850 J m^{-2}). Moreover, the densely crosslinked covalent and ionic networks also stabilized deformation, enabling in vitro and in vivo non-swelling behaviors. Live/dead assay showed 99% cell viability over a period of 60 days.

3.5 Reference

1. Lutolf, M. P. Spotlight on hydrogels. *Nat Mater* 8, 451–453 (2009).
2. Lieleg, O. & Ribbeck, K. Biological hydrogels as selective diffusion barriers. *Trends Cell Biol* 21, 543–551 (2011).
3. Peppas, N. A., Hilt, J. Z., Khademhosseini, A. & Langer, R. Hydrogels in Biology and Medicine: From Molecular Principles to Bionanotechnology. *Adv. Mater.* 18, 1345–1360 (2006).
4. Bertassoni, L. E. et al. Hydrogel bioprinted microchannel networks for vascularization of tissue engineering constructs. *Lab Chip* 14, 2202–2211 (2014).
5. Bodugoz-Senturk, H., Macias, C. E., Kung, J. H. & Muratoglu, O. K. Poly(vinyl alcohol)–acrylamide hydrogels as load-bearing cartilage substitute. *Biomaterials* 30, 589–596 (2009).
6. Sun, J., Keplinger, C., Whitesides, G. M. & Suo, Z. Ionic skin. *Adv. Mater.* 26, 7608–7614 (2014).
7. Roche, E. T. et al. A Bioinspired Soft Actuated Material. *Adv. Mater.* 26, 1200–1206 (2014).
8. Annaidh, A. N., Bruyère, K., Destrade, M., Gilchrist, M. D. & Otténio, M. Characterization of the anisotropic mechanical properties of excised human skin. *J Mech Behav Biomed* 5, 139–148 (2012).
9. Koutroupi, K. S. & Barbenel, J. C. Mechanical and failure behaviour of the stratum corneum. *J Biomech* 23, 281–287 (1990).
10. Arimoto, H. & Egawa, M. Imaging wavelength and light penetration depth for water content distribution measurement of skin. *Skin Res Technol* 21, 94–100 (2015).
11. Kamata, H., Kushihiro, K., Takai, M., Chung, U. & Sakai, T. Non-Osmotic Hydrogels: A Rational Strategy for Safely Degradable Hydrogels. *Angew Chem-ger Edit* 128, 9428–9432 (2016).
12. Kamata, H., Akagi, Y., Kayasuga-Kariya, Y., Chung, U. & Sakai, T. “Nonswellable” Hydrogel Without Mechanical Hysteresis. *Science* 343, 873–875 (2014).
13. Rauner, N., Meuris, M., Zoric, M. & Tiller, J. C. Enzymatic mineralization generates ultrastiff and tough hydrogels with tunable mechanics. *Nature* 543, 407–410 (2017).
14. Gong, J. P., Katsuyama, Y., Kurokawa, T. & Osada, Y. Double-Network Hydrogels with Extremely High Mechanical Strength. *Adv. Mater.* 15, 1155–1158 (2003).
15. Sun, T. L. et al. Physical hydrogels composed of polyampholytes demonstrate high toughness and viscoelasticity. *Nat Mater* 12, 932–937 (2013).

16. Sun, J.-Y. et al. Highly stretchable and tough hydrogels. *Nature* 489, 133–6 (2012).
17. Yang, C. H. et al. Strengthening Alginate/Polyacrylamide Hydrogels Using Various Multivalent Cations. *Acs Appl Mater Inter* 5, 10418–10422 (2013).
18. Lee, K. Y. & Mooney, D. J. Alginate: Properties and biomedical applications. *Prog Polym Sci* 37, 106–126 (2012).
19. Tighe, B. J. The Role of Permeability and Related Properties in the Design of Synthetic Hydrogels for Biomedical Applications. *Brit Polym J* 18, 8–13 (1986).
20. Kabra, B. G., Gehrke, S. H., Hwang, S. T. & Ritschel, W. A. Modification of the dynamic swelling behavior of poly(2-hydroxyethyl methacrylate) in water. *J. Appl. Polym. Sci.* 42, 2409–2416 (1991).
21. Tanaka, M., Mochizuki, A., Ishii, N., Motomura, T. & Hatakeyama, T. Study of Blood Compatibility with Poly(2-methoxyethyl acrylate). Relationship between Water Structure and Platelet Compatibility in Poly(2-methoxyethylacrylate-co-2-hydroxyethylmethacrylate). *Biomacromolecules* 3, 36–41 (2002).
22. Kejlová, K., Labský, J., Jírová, D. & Bendová, H. Hydrophilic polymers—biocompatibility testing in vitro. *Toxicol In Vitro* 19, 957–962 (2005).
23. Chirila, T. V. An overview of the development of artificial corneas with porous skirts and the use of PHEMA for such an application. *Biomaterials* 22, 3311–3317 (2001).
24. Shepherd, J. N. H. et al. 3D Microperiodic Hydrogel Scaffolds for Robust Neuronal Cultures. *Adv. Funct. Mater.* 21, 47–54 (2011).
25. Dziubla, T. D., Torjman, M. C., Joseph, J. I., Murphy-Tatum, M. & Lowman, A. M. Evaluation of porous networks of poly(2-hydroxyethyl methacrylate) as interfacial drug delivery devices. *Biomaterials* 22, 2893–2899 (2001).
26. Dalton, P. D., Flynn, L. & Shoichet, M. S. Manufacture of poly(2-hydroxyethyl methacrylate-co-methyl methacrylate) hydrogel tubes for use as nerve guidance channels. *Biomaterials* 23, 3843–3851 (2002).
27. Yu, H., Fang, Y., Chen, L. & Chen, S. Investigation of redox initiators for free radical frontal polymerization. *Polym. Int.* 58, 851–857 (2009).
28. Coad, J., Stewart, R. & Pedley, K. Encyclopedia of Food and Health. *Article Titles* 461–467 (2016) doi:10.1016/b978-0-12-384947-2.00401-3.
29. Illeperuma, W. R. K., Sun, J.-Y., Suo, Z. & Vlassak, J. J. Force and stroke of a hydrogel actuator. *Soft Matter* 9, 8504–8511 (2013).
30. Rivlin, R. S. & Thomas, A. G. Rupture of rubber. I. Characteristic energy for tearing. *J Polym Sci* 10, 291–318 (1953).
31. Mihaila, S. M. et al. Photocrosslinkable Kappa-Carrageenan Hydrogels for Tissue Engineering Applications. *Adv Healthc Mater* 2, 895–907 (2013).

Chapter 4. Enhanced mechanical properties of functional hydrogels

4.1 Introduction

Hydrogels are crosslinked network polymers with such high hydrophilic moiety that they contain large amounts of water, occupying more than 90 wt. % of the hydrogel. Some hydrogels—including polyelectrolytes, poly(N-isopropyl acrylamide), azo compound polymers, antigen/antibody-grafted polymers, and Belousov–Zhabotinsky (BZ) gels—undergo large volume changes with varying water concentration, as they respond to various stimuli such as pH¹, temperature^{2,3}, light⁴, antigen⁵, and periodic changes in solubility by Ru(bpy)₃^{6,7}. Due to their large volumetric change, some stimulus-responsive hydrogels have been studied as actuator materials^{8–11}. However, the mechanical behaviors of hydrogels restrict their applicability, which is limited by their mechanical behaviors. To elaborate, the previously reported stimulus-responsive hydrogels are unsuitable for actuators against gravity because they exhibit brittle properties and a low fracture toughness of approximately 20 J m⁻².

Various types of hydrogels, including fiber-reinforced gel¹² and silica nanoparticle-grafted hydrogel¹³, have been developed in attempts to enhance the fracture toughness. One study achieved a remarkable enhancement of fracture energy greater than 1,000 J m⁻² by forming a double-network structure¹⁴. Double networks contain interpenetrated networks between covalently crosslinked short and long chains. In another work, Sun and colleagues reported the synthesis of hydrogels from polymers to form ionically and covalently crosslinked networks, and they attributed the resulting toughness of the gel to the synergy of two mechanisms: crack bridging

by the network of covalent crosslinks and energy dissipation by unzipping the network of ionic crosslinks¹⁵. In that study, an extreme fracture toughness of approximately $9,000 \text{ J m}^{-2}$ was achieved by introducing reversible ionic crosslinks of alginate into covalent crosslinks of polyacrylamide instead of interpenetrating two strong, covalently crosslinked networks¹⁵. They also reported highly stiff and tough hydrogels by fully utilizing ionic crosslinking sites of alginate chains¹⁶. However, although these tough gels exhibited excellent mechanical properties, they were not stimulus responsive.

In a recent study, a topological hydrogel with sliding-ring crosslinkers was synthesized to enhance the mechanical properties of actuating materials¹⁷. This hydrogel exhibited high stretchability, which was achieved by using polyrotaxane sliding rings that can move along the chain. It also demonstrated thermo-sensitive properties and high stretchability. Stretchability is an important issue for high fracture toughness, as it facilitates reliable device fabrication, but the actual utilization of this hydrogel has been impeded by its poor fracture toughness, because the required fracture toughness of a hydrogel for an actuator or artificial muscle is $200\text{--}500 \text{ J m}^{-2}$ ^{18,19}. Modulus also plays a critical role in achieving practical actuation performance by enhancing fracture toughness; the actuation force increases with increasing modulus²⁰. To date, there have been very few reports of hydrogel-based actuators with decent mechanical properties, and the hydrogels that have been reported have not demonstrated pragmatic actuation performance.

In this study, we fabricated a hydrogel-based actuator with a large actuation force by means of enhanced modulus and fracture toughness. Specifically, poly(N-isopropylacrylamide) hydrogel was used as a thermo-sensitive actuator material and covalently crosslinked networks of the PNIPAAm hydrogel were interpenetrated

with ionically crosslinking by alginate networks, which helped improve the actuator's mechanical properties, and its modulus and fracture toughness in particular. These thermally active hydrogels with a tough and large actuation force that we have developed demonstrate practical feasibility for the fabrication of reliable hydrogel-based devices.

4.2 Experimental section

4.2.1 Gel preparation

The interpenetrating network (IPN) gels were prepared by dissolving alginate and NIPAAm monomer powders in distilled water. The water concentration, $\left(\frac{\text{water wt.}}{(\text{alginate+NIPAAm+water})\text{wt.}} \times 100\right)$ was fixed at 89.59 wt. % throughout the experiments for the IPN, and the polymer ratios were varied by mixing different amounts of alginate and NIPAAm powders. MBAA 0.17 wt. % and APS 0.95 wt. %, with respect to the weight of the NIPAAm monomer, were added as a crosslinker for NIPAAm and an initiator, respectively. Finally, after degassing in a vacuum chamber, calcium sulfate slurry 22.77 wt. % with respect to the weight of the alginate monomer and TEMED 2.5 wt. % with respect to the weight of the NIPAAm monomer were added as the ionic crosslinker for the alginate and accelerator.

Next, the solutions were poured into a glass mold with a $75.0 \times 150.0 \times 3.0 \text{ mm}^3$ -sized vacancy and covered with a 3 mm-thick transparent glass plate. The gels were cured by an ultraviolet light crosslinker (UVC 500, Hoefer, Holliston, MA, USA) with 8 W power and a 254 nm wavelength at room temperature for 4 h. To avoid heating the gel sample during gelation, the UV crosslinker was kept approximately 10 cm away from the gel sample. Then, before performing the mechanical tests, the

gels were left in a humid box for 1 day to stabilize the reactions.

The IPN gels are hereafter referred to as $P_1-x_1-y_1/P_2-x_2-y_2$, where P_i , x_i , and y_i ($i = 1, 2$) are the abbreviated polymer name (i.e., PNIPAAm), the weight concentration of the monomer in wt. % with respect to the weight of water (e.g., $x_1 = \frac{\text{PNIPAAm wt.}}{\text{Water wt.}} \times 100$) and the crosslinker concentration in wt. % with respect to the monomer of the i_{th} network, (e.g., $y_1 = \frac{\text{MBAA wt.}}{\text{PNIPAAm wt.}} \times 100$) respectively.

4.2.2 Mechanical test preparation

Before the mechanical tests, the surfaces of the hydrogels were dried with N_2 gas for 1 min to remove water. Four stiff polyacrylate plates were glued with superglue to clamp the gel. In the end, $75.0 (L) \times 5.0 (H_0) \times 3.0 (t) \text{ mm}^3$ test specimens were prepared for the tests. All mechanical tests were performed at room temperature on a tensile machine (Instron model 3342, Norfolk County, MA, USA) with a 500 N-capacity load cell, and the nominal stress and stretch were recorded. The stretch rate was kept constant at $\dot{\lambda} = 2 \text{ min}^{-1}$

4.2.3 Thermo-sensitive behaviors test preparation

A $20 \times 5 \times 3 \text{ mm}^3$ sample of the hybrid gel was prepared to investigate the dynamic length. Free swelling in the same concentration of calcium ion was conducted to protect against the loss of Ca^{2+} from the gel at 20°C for 1 day. After measuring the length of the fully swollen hydrogel, the gel was submerged in thermostatic 50°C water in a submergible clamp kit. The dynamic length of the hybrid gel was then recorded as a function of submerged time in the range from 20°C to 50°C .

Pure PNIPAAm gel and hybrid gel samples were cut into sizes of $20 \times 5 \times 3 \text{ mm}^3$

to observe the equilibrium length. Free swelling was examined under the same circumstances via a dynamic length-measurement test. The equilibrium lengths of the hydrogels at each temperature were measured in the range from 20 °C to 50 °C. Each temperature was kept constant for 4 h to ensure that the sample gels reached the equilibrium state, and the equilibrium length of the hydrogels was then measured.

Hybrid gels with various weight ratios of PNIPAAm/(PNIPAAm + alginate) were prepared to record the equilibrium lengths of the hybrid gels and compare the influence of the amount of alginate on equilibrium length. Hybrid gel samples with the dimensions of $20 \times 5 \times 3 \text{ mm}^3$ were subjected to an equilibrium length-measurement test with the same test conditions as those previously described.

4.3 Results and Discussion

To fabricate the hydrogel-based actuator to be tested in this work, poly(N-isopropylacrylamide) hydrogel was used as a thermo-sensitive actuator material. N-isopropylacrylamide has the hydrophobic moiety of the isopropyl group, whereas acrylamide only has the hydrophilic moiety of the amide group. The hydrophobic moiety of the isopropyl group impedes the hydrogen interaction between water molecular and hydrophilic moiety depending on temperature, which results in a thermo-sensitive phase transition associated with the LCST (Lower Critical Solution Temperature) ²¹. This phase transition phenomenon facilitates hydrogel-based actuator operation. However, as this pure PNIPAAm hydrogel exhibits soft and brittle properties, it could only exhibit deformation without the application of external force on an object as an actuator. To enhance the mechanical properties, these covalently crosslinked networks of the PNIPAAm hydrogel were

interpenetrated with ionic crosslinks by alginates. Alginates are polymeric carbohydrate molecules, and their structures are linearly copolymer, with blocks of mannuronate (M unit) and guluronate (G unit) that are consecutively arranged in M blocks, G blocks, and alternating M and G blocks ¹⁵. The G blocks in one alginate molecule can be ionically crosslinked with various cations. PNIPAAm and alginate-based interpenetrating network hydrogel can be enhanced through the synergy of two mechanisms: crack bridging by a covalently crosslinked network of PNIPAAm by an MBAAm crosslinker, and energy dissipation by unzipping the ionically crosslinked network of alginate by a Ca^{2+} ion crosslinker ¹⁵.

Fig. 4 demonstrates the enhancements in the mechanical properties of the hybrid gels that have been achieved through the formation of interpenetrating networks. As shown in Figure 1a–d, a cylindrically shaped pure PNIPAAm gel was prepared and swollen in 20 °C water for a day. After this swelling period, the pure gel had a length of 20 mm and a diameter of 10 mm (Fig. 4.1 a). To begin, a 2 g brass dead weight was glued onto one end of the pure PNIPAAm gel, at which point the gel was hung from the ceiling. Next, the pure gel was stretched by gravity to 1.4 times its initial length at 20 °C (Fig. 4.1. b). The temperature of the water was then increased to 50 °C to monitor the thermal actuation in However, because the pure gel was brittle, the gel ruptured during loading when 3 g of 50 °C water for a day. After shrinkage in 50 °C water for 1 day, the pure gel was able to lift dead weight was used, as shown in Fig. 4.1. c. However, because the pure gel was brittle, the gel ruptured during loading when 3 g of dead weight was used, as shown in in Fig. 4.1. d. In contrast, PNIPAAm–alginate hybrid gel is tough, and it is therefore capable of lifting a heavier dead weight than pure gel. The hybrid gel that was fully swollen in 20 °C water for 1 day was prepared with a length of 20 mm and a diameter of 10 mm, and it is shown

in its initial state in Fig. 4.2. a. The hybrid gel was stretched to 1.5 times its original length with a 7 g brass dead weight (Fig. 4.2. b). As shown in Fig. 4.2. c, the gel was shrunk to 20 mm from 30 mm length in 50 °C water due to the thermos-sensitive behavior. The hybrid gel was kept intact with 7 g of dead weight during the loading and actuation processes. The results showed that fracture toughness is an essential component to consider for thermos-sensitive materials to prevent crack propagation during operation. PNIPAAm–alginate hybrid gels were synthesized with various weight ratios of PNIPAAm to (PNIPAAm plus alginate) and subjected to tensile tests and fracture tests to measure their mechanical properties.

For tensile testing, an un-notched hybrid gel was glued to four stiff polyacrylate clamps, resulting in specimens with initial dimensions of width $L = 75$ mm and thickness $t = 3$ mm, and the distance between the two clamps was $H_0 = 5$ mm. The specimen was then stretched to rupture using a tensile machine (Instron model 3342). The stretch rate was kept constant $\dot{\lambda} = 2 \text{ min}^{-1}$.

Fig. 4.3 a shows the stress–stretch curves of the hybrid gels with various weight ratios of PNIPAAm to (PNIPAAm plus alginate), as measured by the tensile tests. The stretch, λ , is defined as the distance between the two clamps when the gel is deformed divided by the distance when the gel is at a weight ratio of 96 wt. %, which is close to that of pure PNIPAAm gel; the hybrid gel exhibited the lowest elastic modulus of 4.26 kPa with the highest stretchability of 4.56. With increasing alginate, stretch decreased proportionally, whereas the modulus increased, as shown in Fig. 4.3 b. Fracture tests were performed with notched samples. The initial notches were made by a razor blade while controlling the initial notch size $C_0/L \approx 0.5$. The onset of crack propagation was monitored by a camera during an instance of uniaxial stretching. Fig. 4.4 a shows the critical stretches of onset crack propagation for

different hybrid gels at various weight ratios. When the proportion of alginate was increased, the critical stretch of crack propagation was decreased. The method introduced by Rivlin and Thomas²² was used to determine the fracture toughness of a gel. The fracture toughness was calculated from the fracture energy equation, where L and t are the width and thickness of undeformed samples, respectively, and $U(H_c)$ is the area under the stress–stretch curves from zero to critical stretch (H_c). Rivlin–Thomas’ methods are explained in further detail in Fig. 4.5. The measured fracture toughness is plotted in Fig. 4.4 b as a function of the weight ratios of PNIPAAm/(PNIPAAm + alginate). The fracture toughness of the hybrid gel reached a maximum value of 697.08 J/m² at 88.89 wt. %; this was 58 times higher than that of pure PNIPAAm gel, which is 12 J/m². Further, the measured toughness of the hybrid gel is higher than that of muscles (e.g., horse quadriceps muscle¹⁸ and salmon muscle¹⁹ have fracture toughness values ranging between 200 and 500 J/m²).

Next, we investigated the thermo-sensitive behaviors of the prepared hybrid gels. To this end, a hybrid gel of PNIPAAm-10.33-0.17/alginate-1.29-22.77 was fully swollen in 20 °C water for a day and cut into a test size with the dimensions of 20 × 5 × 3 mm³ by a laser cutter. The gel was then submerged into 50 °C water. The dynamic length in 50 °C water, $\ell(50\text{ °C})$, of the hybrid gel was monitored through a camera. Figure 3a plots the dynamic swelling ratio in 50 °C water, $\ell(50\text{ °C})/L(20\text{ °C})$, of the hybrid gel as a function of submerged time, t . The dynamic length of the gel was normalized with length at an equilibrium state in 20 °C water, $L(20\text{ °C})$. The dynamic swelling ratio of the hybrid gel decreased as a function of submerged time and reached an equilibrium state after 100 min, which is near the theoretical self-diffusion time of 94 min in 50 °C water. The theoretical self-diffusion time of thermo-sensitive hydrogel caused by the diffusion of water molecules was calculated

using the following diffusion equation, $\ell = \sqrt{Dt}$, where the gel size was $20 \times 5 \times 3$ mm³, the water diffusion distance was $\ell = 1.5$ mm, and the self-diffusion coefficient of water at 50 °C was $D_{50^\circ\text{C}} = 3.983 \cdot 10^{-9} \text{ m}^2/\text{s}^{-1}$ ²³. As illustrated in Fig. 4.6, a transparent hybrid gel of PNIPAAm-10.33-0.17/alginate-1.29-22.77 was fully swollen in 20 °C water. The equilibrium length of the gel in 20 °C water is called $L(20^\circ\text{C})$. After being submerged in 50 °C water, the hybrid gel reached another equilibrium state at 50 °C, where it had a length of $L(50^\circ\text{C})$ and exhibited an opaque appearance (Fig. 4.7). The equilibrium lengths of the pure gel and hybrid gel at temperature T , $L(T)$, are compared in Fig. 4.8. To obtain each data point, the sample was stored under the designated temperature for 4 h to reach an equilibrium state. The equilibrium length of the gels at temperature T , $L(T)$, was normalized with the length at an equilibrium state in 20 °C was called the equilibrium swelling ratio. The equilibrium swelling ratio was not changed for either the hybrid or pure gels until 32 °C. The pure gel and hybrid gel both underwent phase transitions in a similar temperature range from 32 to 35 °C, which is consistent with the values reported by previous studies²⁴. The equilibrium swelling ratio of hybrid gel reached a steady value of 0.52 after the phase transition, which is higher than that of pure gel, 0.35. The volume change in the hybrid gel was lower than that of pure gel. The equilibrium swelling ratios of hybrid gels at a variety of weight ratios are plotted in Fig. 4.9. The volume change in the hybrid gel was decreased when the proportion of alginate was increased.

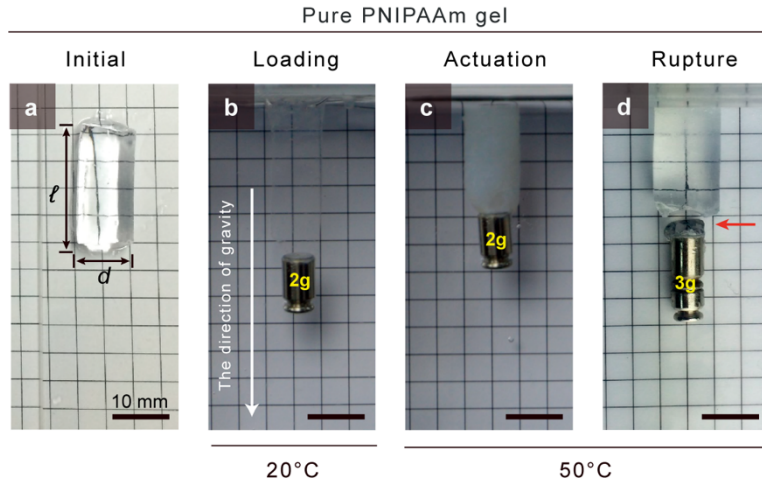


Figure 4.1 Pure active materials are weak.

(a) Pure PNIPAAm gel was submerged into 20 °C water for 1 day and cut into an initial size of $\ell = 21$ mm with a cylindrical shape ($d = 10$ mm). (b) 2 g of brass dead weight was glued to one end of the pure PNIPAAm gel, which was then hung from the ceiling. The gel was stretched by gravity in 20 °C water. (c) Pure gel with a 2 g brass dead weight was shrunk in 50 °C water for 1 day. (d) Pure PNIPAAm gels were ruptured by a 3 g brass dead weight in 20 °C water (arrow identifies ruptured area in the gel).

PNIPAAm-alginate hybrid gel

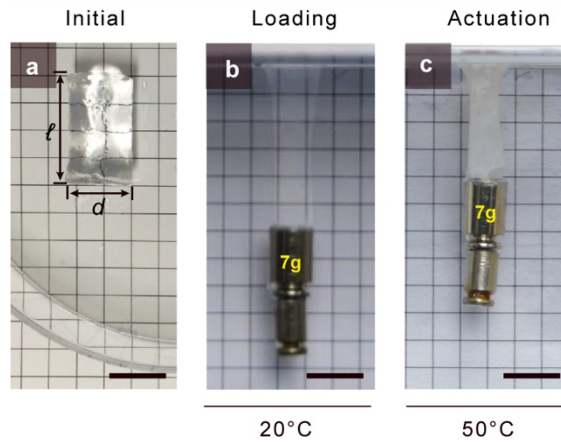


Figure 4.2 Active materials must be tough.

(a) PNIPAAm-alginate hybrid gel fully swollen in 20 °C water for a day and cut into a test size of $l = 20$ mm with a cylindrical shape ($d = 10$ mm). (b) Hybrid gel capable of sustaining a 7 g brass dead weight in 20 °C water. (c) Hybrid gel showing thermal actuation against a 7 g brass dead weight in 50 °C water. The gel remained intact during actuation.

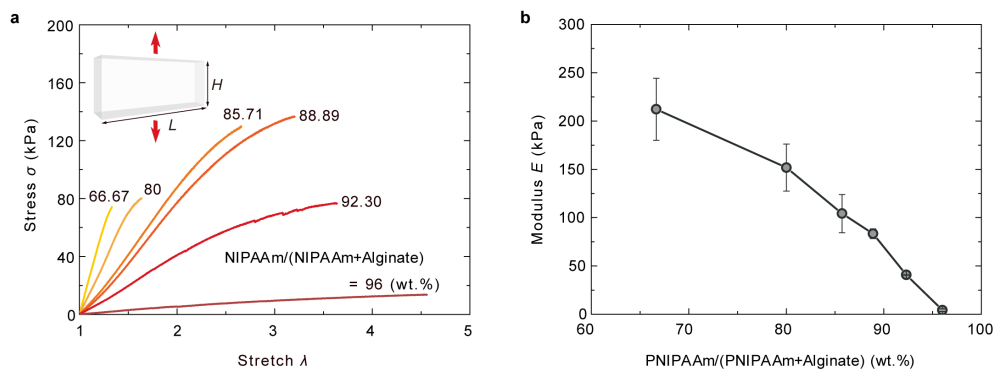


Figure 4.3 Tensile tests of PNIPAAm-alginate hybrid gel.

(a) Un-notched hybrid gel stretched to rupture for a tensile test. Hybrid gels with various weight ratios of PNIPAAm/(PNIPAAm + alginate) were tested. The sample design shown in the inset ($L/H_0 \geq 20$) was used for the tensile tests. The stretch rate was kept constant at $\dot{\lambda} = 2 \text{ min}^{-1}$. (b) The elastic modulus was calculated from the stress–stretch curves in (a) and plotted as a function of the weight ratio of PNIPAAm/(PNIPAAm + alginate). The elastic modulus was increased when the proportion of alginate increased.

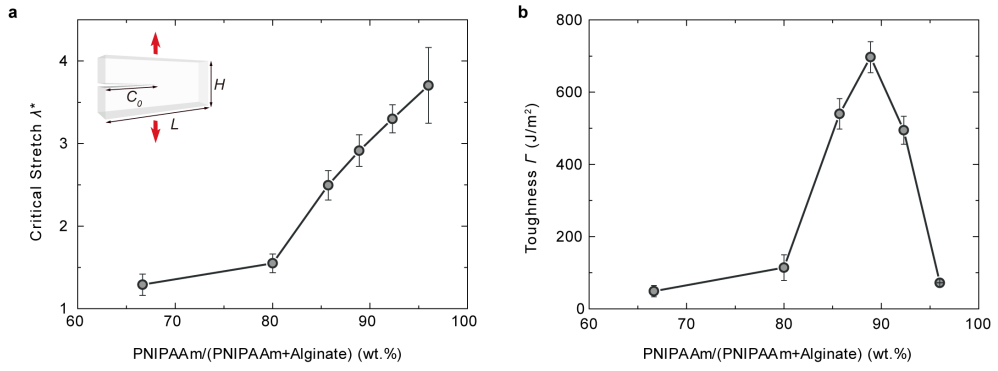


Figure 4.4 Fracture tests of PNIPAAm-alginate hybrid gel.

(a) Fracture tests were performed on the notched samples shown in the inset ($C_0/L \approx 0.5$). Onset crack propagation was monitored by a camera during uniaxial stretching. Cracks tended to propagate earlier with increasing amounts of alginate.

(b) The fracture toughness was plotted as a function of the weight ratio of PNIPAAm/(PNIPAAm + alginate). The hybrid gel has a maximum toughness of approximately 700 J/m² at 88.89 wt. %. The weight of the covalent crosslinker, MBAA, was fixed at 0.00167; the weight of the ionic crosslinker, CaSO₄, was fixed at 0.2327 (water content: 89.59 wt. %)

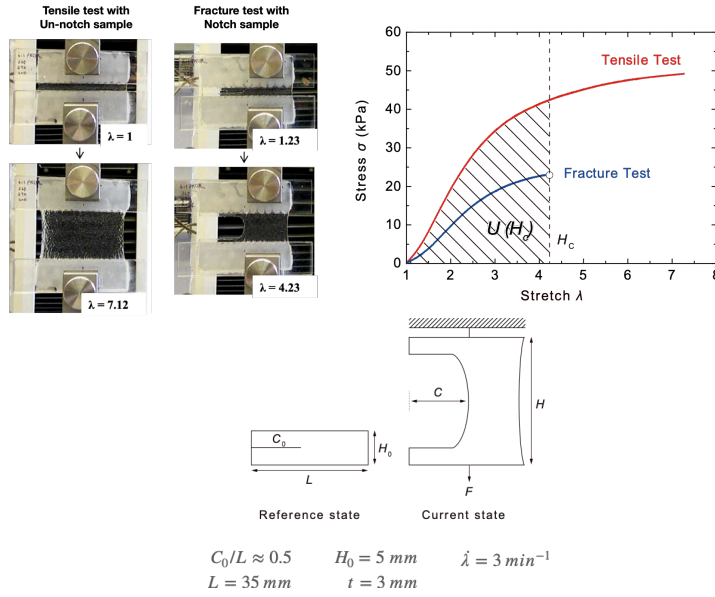


Figure 4.5 Fracture toughness measurement of hybrid gel.

Notched and un-notched samples were prepared for tensile tests and fracture tests. The un-notched sample was pulled to measure the force-length curve. The initial samples have a width $L = 75 \text{ mm}$ and a thickness $t = 3 \text{ mm}$, and the distance between the two clamps was $H_0 = 5 \text{ mm}$. When the two clamps were pulled to a distance H , the area beneath the force-length curve gave the work done by the applied force, $U(H)$. For a fracture test, the notched sample was prepared using a razor blade to cut a 40 mm-long notch into the gel. The notched sample was pulled, and pictures were taken at a rate of $\sim 30 \text{ frames/s}$ to record the critical distance between the clamps, H_c , when the notch turned into a running crack. The fracture energy was calculated by $\Gamma = U(H_c)/Lt \text{ J m}^{-2}$

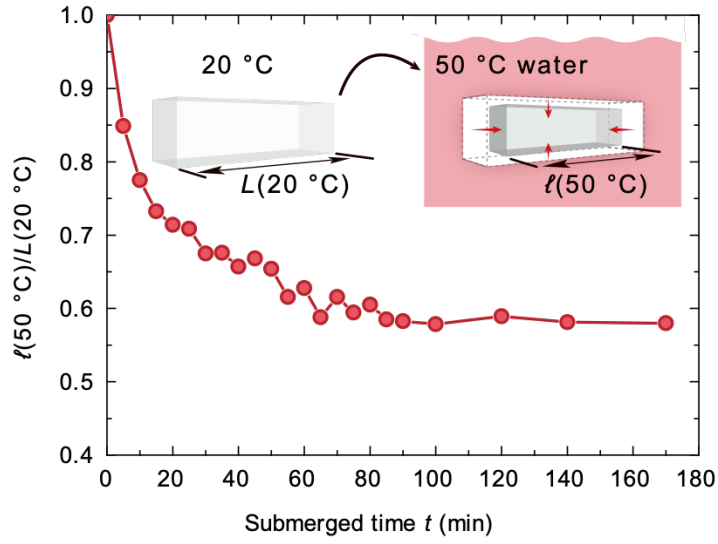


Figure 4.6 Thermo-sensitive behaviors of hybrid gel.

$20 \times 5 \times 3 \text{ mm}^3$ PNIPAAm–alginate hybrid gel, which was fully swollen in $20\text{ }^{\circ}\text{C}$ water, was submerged into $50\text{ }^{\circ}\text{C}$ water. Dynamic length in $50\text{ }^{\circ}\text{C}$ water, $\ell(50\text{ }^{\circ}\text{C})$, was captured as a function of submerged time. The dynamic swelling ratio, $\ell(50\text{ }^{\circ}\text{C})/L(20\text{ }^{\circ}\text{C})$, of a hybrid gel reached an equilibrium state after 100 min, which is near the theoretical self-diffusion time of 94 min in $50\text{ }^{\circ}\text{C}$ water.

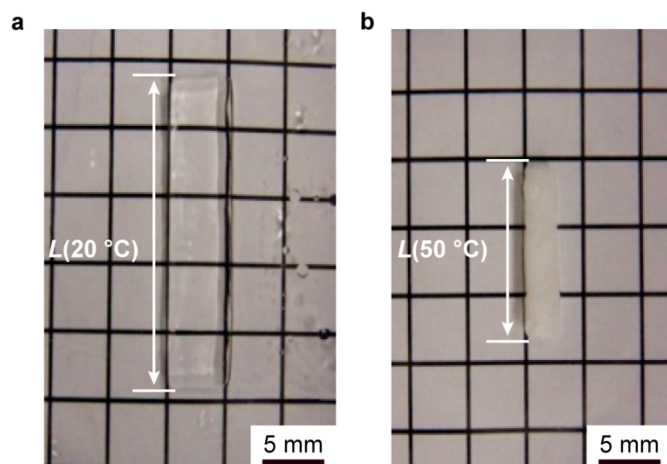


Figure 4.7 Phase transition.

Hybrid gel of PNIPAAm-10.33-0.17/alginate-1.29-22.77 fully swollen in 20 °C water. (a) Equilibrium length of the gel in 20 °C water is called $L(20\text{ }^{\circ}\text{C})$. (b) After being submerged in 50 °C water, the gel reached another equilibrium state with a length of $L(50\text{ }^{\circ}\text{C})$.

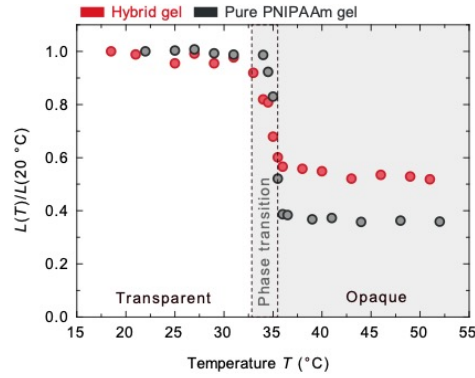


Figure 4.8 Comparison of equilibrium lengths at temperature T .

For each data point, the sample was stored under a designated temperature for 4 h to reach an equilibrium state. Both pure and hybrid gels underwent phase transition in a similar temperature range from 32 to 35 °C. However, the equilibrium swelling ratios, $L(T)/L(20\text{ °C})$, of pure gel and hybrid gel reached steady values of 0.35 and 0.52, respectively.

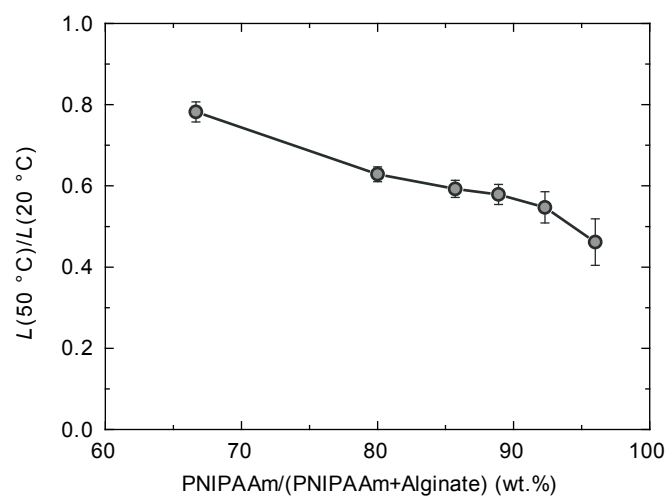


Figure 4.9 Equilibrium swelling ratio.

Equilibrium swelling ratio of hybrid gel plotted as a function of weight ratios of PNIPAAm/(PNIPAAm + alginate).

4.4 Conclusion

In conclusion, we have developed a hydrogel-based actuator with a tough and large actuation force by using poly(N-isopropylacrylamide) hydrogels as thermo-sensitive actuator materials and interpenetrating network structures between the covalently crosslinked poly(N-isopropylacrylamide) and ionically crosslinked alginate. This interpenetrating structure enhanced the mechanical properties of the hybrid gels. By examining these thermally active hydrogels with a tough and large actuation force, we successfully demonstrated their practical feasibility for the fabrication of reliable hydrogel-based devices. The stiffness and fracture energy of the resultant hybrid hydrogel were enhanced by factors of 50 and 14, respectively. In particular, the hybrid gel generated an actuation force up to seven times larger than that of pure gel. These excellent mechanical properties are attributed to the enhanced elastic modulus and energy dissipation in the hybrid gel. Remarkably, the actuating motion of the hybrid hydrogel was available due to a comparable volumetric change with pure PNIPAAm gel. This work demonstrates a simple and diverse fabrication approach that can achieve enhanced mechanical performances for a variety of functional hydrogels, and which extends potential applications of hydrogels in the tissue engineering, artificial muscles, and sensor fields.

4.5 Reference

1. Beebe, D. J. et al. Functional hydrogel structures for autonomous flow control inside microfluidic channels. *Nature* 404, 588–590 (2000).
2. Kim, Y. S. et al. Thermoresponsive actuation enabled by permittivity switching in an electrostatically anisotropic hydrogel. *Nat Mater* 14, 1002–1007 (2015).
3. Xia, L.-W. et al. Nano-structured smart hydrogels with rapid response and high elasticity. *Nat Commun* 4, 2226 (2013).
4. Takashima, Y. et al. Expansion-contraction of photoresponsive artificial muscle regulated by host-guest interactions. *Nat Commun* 3, 1270 (2012).
5. Miyata, T., Asami, N. & Uragami, T. A reversibly antigen-responsive hydrogel. *Nature* 399, 766–769 (1999).
6. Mao, Z., Kuroki, M., Otsuka, Y. & Maeda, S. Contraction waves in self-oscillating polymer gels. *Extreme Mech Lett* 39, 100830 (2020).
7. Sato, K., Enomoto, T., Akimoto, A. M. & Yoshida, R. Fabrication of Self-Oscillating Gels by Polymer Crosslinking Method and Analysis on Their Autonomous Swelling-Deswelling Behaviors. *Gels* 8, 267 (2022).
8. Lee, H., Xia, C. & Fang, N. X. First jump of microgel; actuation speed enhancement by elastic instability. *Soft Matter* 6, 4342–4345 (2010).
9. Kim, J., Hanna, J. A., Byun, M., Santangelo, C. D. & Hayward, R. C. Designing Responsive Buckled Surfaces by Halftone Gel Lithography. *Science* 335, 1201–1205 (2012).
10. Hu, Z., Zhang, X. & Li, Y. Synthesis and Application of Modulated Polymer Gels. *Science* 269, 525–527 (1995).
11. O’Grady, M. L., Kuo, P. & Parker, K. K. Optimization of electroactive hydrogel actuators. *Acs Appl Mater Inter* 2, 343–6 (2010).
12. Illeperuma, W. R. K., Sun, J.-Y., Suo, Z. & Vlassak, J. J. Fiber-reinforced tough hydrogels. *Extreme Mech Lett* 1, 90–96 (2014).
13. Wang, Q., Hou, R., Cheng, Y. & Fu, J. Super-tough double-network hydrogels reinforced by covalently compositing with silica-nanoparticles. *Soft Matter* 8, 6048 (2012).
14. Gong, J. P., Katsuyama, Y., Kurokawa, T. & Osada, Y. Double-Network Hydrogels with Extremely High Mechanical Strength. *Adv. Mater.* 15, 1155–1158 (2003).
15. Sun, J.-Y. et al. Highly stretchable and tough hydrogels. *Nature* 489, 133–6 (2012).

16. Kim, Y.-W., Kim, J. E., Jung, Y. & Sun, J.-Y. Non-swellable, cytocompatible pHEMA-alginate hydrogels with high stiffness and toughness. *Mater Sci Eng C* 95, 86–94 (2019).
17. Imran, A. B. et al. Extremely stretchable thermosensitive hydrogels by introducing slide-ring polyrotaxane cross-linkers and ionic groups into the polymer network. *Nat Commun* 5, 5124 (2014).
18. King, M. J. Fracture energy during slicing of frozen meat by a vibrating knife. *Meat Sci* 46, 387–399 (1997).
19. Anderson, P. S. L. The effects of trapping and blade angle of notched dentitions on fracture of biological tissues. *J Exp Biology* 212, 3627–32 (2009).
20. Illeperuma, W. R. K., Sun, J.-Y., Suo, Z. & Vlassak, J. J. Force and stroke of a hydrogel actuator. *Soft Matter* 9, 8504–8511 (2013).
21. Rivlin, R. S. & Thomas, A. G. Rupture of rubber. I. Characteristic energy for tearing. *J Polym Sci* 10, 291–318 (1953).
22. Wu, C. & Wang, X. Globule-to-Coil Transition of a Single Homopolymer Chain in Solution. *Phys Rev Lett* 80, 4092–4094 (1998).
23. Holz, M., Heil, S. R. & Sacco, A. Temperature-dependent self-diffusion coefficients of water and six selected molecular liquids for calibration in accurate ¹H NMR PFG measurements. *Phys Chem Chem Phys* 2, 4740–4742 (2000).
24. Otake, K., Inomata, H., Konno, M. & Saito, S. Thermal analysis of the volume phase transition with N-isopropylacrylamide gels. *Macromolecules* 23, 283–289 (1990).

Bibliography

1. Publications

1. Kim, Y.-W. & Sun, J.-Y. Anisotropic conductive hydrogels in controlled microstructures. *In preparation*.
2. Kim, Y.-W., Kim, D. Y. & Sun, J.-Y. Fracture toughness and blocking force of temperature-sensitive PolyNIPAAm and alginate hybrid gels. *Gels* 8, 324 (2022).
3. Kim, Y.-W., Kim, J. E., Jung, Y. & Sun, J.-Y. Non-swellable, cytocompatible pHEMA-alginate hydrogels with high stiffness and toughness. *Mater. Sci. Eng. C* 95, 86–94 (2019).
4. Bae, S.W., Kim Y.-W., Sun, J.-Y., Kwon, S. Robust hydrogels-integrated microsystems enabled by enhanced interfacial bonding strength. *BioRxiv*
5. Saygili, E. et al. Bilayered laponite/alginate-poly(acrylamide) composite hydrogel for osteochondral injuries enhances macrophage polarization: An in vivo study. *Biomaterials Adv.* 134, 112721 (2022).
6. Saygili, E. et al. An alginate-poly(acrylamide) hydrogel with TGF- β 3 loaded nanoparticles for cartilage repair: Biodegradability, biocompatibility and protein adsorption. *Int. J. Biol. Macromol.* 172, 381–393 (2021).
7. Ma, J. Lin, Y., Kim, Y.-W. et al., Liquid Metal Nanoparticles as Initiators for Radical Polymerization of Vinyl Monomers. *Acs Macro. Lett.* 8, 1522–1527 (2019)
8. Lee, H.-H., Kim, Y.-W., Woo, J., Park, H., Hur, K., Suo, Z. Fast healing of ionic bonds in tough hydrogels under an acoustic excitation. *Extreme Mech. Lett.* 33, 100572 (2019).

9. Lee, Y., Cha, S.H., Kim, Y.-W., Choi, D., Sun, J.-Y. Transparent and attachable ionic communicators based on self-cleanable triboelectric nanogenerators. *Nat. Commun.* 9, 1804 (2018).

2. R&D projects

1. “Synthesis of a novel stiff hydrogel for cartilage tissue engineering functionalized with nanoparticles fabricated by using a microfluidic platform along with iv vivo studies”, International Cooperation Program funded by National Research Foundation of Korea, 2017.11 – 2019.10
2. "Development of 3D printed vascularized skeletal organ implant for rapid bone regeneration". Convergence Research between Engineering and Medical Schools funded by Seoul National University, 2017.04 – 2018.03
3. “Hydrogel with improved modulus and medical uses thereof”, Cooperative Project funded by ILJIN Holdings, 2015.07 – 2016.06

3. Patent

Jeong-Yun Sun, Yong-Woo Kim, Kyung Sik Noh, Ki Joon Kim. Hydrogel with improved modulus and medical uses thereof. Korea Patent (10-2016-0092850)

4. Conference presentations

1. Kim, Y.-W., Kim, J. E., Jung, Y. & Sun, J.-Y. Non-swellable, cytocompatible pHEMA-alginate hydrogels with high stiffness and toughness. The Polymer Society of Korea Annual Fall Meeting, Gyeongju, Korea (2018)^[1]_{SEP}
2. Kim, Y.-W., Kim, J. E., Jung, Y. & Sun, J.-Y. Non-swellable, cytocompatible

pHEMA-alginate hydrogels with high stiffness and toughness. 19th Korea-Japan student symposium, KAIST, Daejeon, Korea (2018)

3. Kim, Y.-W., Kim, J. E., Jung, Y. & Sun, J.-Y. Non-swellable, cytocompatible pHEMA-alginate hydrogels with high stiffness and toughness. Materials Research Society (MRS) Spring Meeting, Phoenix, USA (2018)

4. Kim, Y.-W., Sun, J.-Y. Non-swellable, cytocompatible pHEMA-alginate hydrogels with high stiffness and toughness. 3rd novel fluidic technologies workshop with an emphasis on tissue engineering, Izmir, Turkey (2018)

5. Kim, Y.-W., Sun, J.-Y. Non-swellable, cytocompatible pHEMA-alginate hydrogels with high stiffness and toughness. 18th Korea-Japan student symposium, Dohuku, Japan (2017)

4. Award

Bronze Prize, Young Researchers Excelling in Novel Fluidic Award. 3rd novel fluidic technologies workshop with an emphasis on tissue engineering. Izmir, Turkey (2018)

Abstract in Korean

하이드로젤은 다량의 물을 보유하고 있는 친수성 고분자 네트워크이다. 높은 수분 함량은 하이드로젤이 다양한 중합체와 염을 용해시켜 생리학적 조건과 유사하게 만든다. 구조적 및 기계적 제어성은 젤을 생물학적 조직의 구조적 및 기계적 특성과 유사하게 만든다. 하이드로젤은 소수성 물질에 비해 인간의 면역 반응을 감소시키는 친수성을 가지고 있다. 따라서, 하이드로젤은 다른 물질과 비교하여 생체적합성이 더 높을 수 있다. 하이드로젤의 이러한 특성 때문에, 하이드로젤은 표피 센서, 이식 장치, 조직 대체, 약물 전달 및 상처 치유와 같은 광범위한 분야에 사용된다.

첫 번째 장에서는 바람직한 생체 전자 성능 및 기능성을 달성하기 위해 정렬, 결정성, 기공 크기, 상분리, 점도 등의 미세 구조를 조절함으로써 하이드로젤에서의 높은 전기적 이방성을 달성하였다.

두 번째 장에서는 공유 및 이온성 가교 네트워크를 상호 침투하여 탄성계수와 파괴인성이 높은 비팽윤 하이드로젤을 설계했다. 이온 가교 사이트를 충분히 활용하여 탄성율을 높이고, 이온 네트워크에 의한 에너지 분산과 공유 네트워크에 의한 크랙-브릿징 사이의 시너지 효과로 탄성계수를 향상시킨다. 하이드로젤의 비팽윤 거동은 공유 및 이온 가교를 고밀화하여 달성된다. 하이브리드 하이드로젤은 높은 탄성 계수 (최대 108 MPa)와 높은 파괴 인성 (최대 8850 J m^{-2})를 보여준다.

또한, 세 번째 장에서는 기능성을 잃지 않고 파괴 인성을 강화하기 위해 강화 메커니즘을 기능성 폴리머에 적용할 수 있음을

입증했다. 공유 가교 폴리(N-이소프로필 아크릴아미드)와 이온 가교 알긴산염 사이에 상호 침투 네트워크를 형성하여 온도 반응성이 큰, 높은 파괴인성과 온도에 민감한 하이드로겔을 합성했다. 온도 감응성 물질로는 폴리(N-이소프로필아크릴 아미드)를 사용하였으며, 알긴산염을 사용하여 하이드로겔의 기계적 물성을 향상시켰다. 하이브리드 겔 내의 향상된 탄성 계수 및 에너지 분산으로 인해 순수 PNIPAAm 하이드로겔에 비해 파괴인성이 60배 증가하였다.

핵심어: 전기적 비등방성, 전도성 하이드로겔, 고탄성 하이드로겔, 높은 파괴인성 하이드로겔, 비팽윤성 하이드로겔

학번: 2014-22514